

## Chapter 4

# Overmodulation in Voltage Feedforward Controlled Drives

### 4.1 Introduction

In the previous section the linear modulation range behavior of the modern carrier based PWM methods was studied in detail. Their performance characteristics were analytically derived and graphically illustrated. It was shown several modern PWM methods exhibit superior performance characteristics and their application areas were identified. However, all the carrier based PWM methods provide a linear relationship between the reference and the output voltages within a limited range.

The linear voltage range of a PWM-VSI drive is mainly determined by the modulator characteristics. Using the modulation index definition of the previous chapter, full voltage utilization (six-step operating mode) occurs at  $M_i = 1$ . Normalizing the triangular wave peak-to-peak signal magnitude to  $V_{dc}$ , it follows that SPWM's linear modulation range ends at  $V_{1m} = \frac{V_{dc}}{2}$ , a modulation index

of  $M_{imax[SPWM]} = \frac{\pi}{4} \approx 0.785$ . Inverter blanking time and minimum-pulse-width constraints can further reduce the range of linearity by a considerable amount. As a result, the voltage linearity of a drive, for example, in the SPWM case, can be lost at as low a value as 70% of the six-step voltage, i.e. 0.7 modulation index. Figure 4.1 illustrates the typical linear and nonlinear range modulation waveforms of the SPWM method, and switching device gate logic signals. The portion of the modulation wave having a larger magnitude than the triangular wave peak value remains unmodulated, and the gate signals remain on or off for a full carrier cycle leading to a nonlinear reference-output voltage relationship.

The voltage linearity of a modulator can be significantly increased by injecting a zero sequence signal. For example, in the SVPWM case, the theoretical limit can be easily calculated by evaluating the modulation signal at the  $30^\circ$  point (see Fig. 3.7 SVPWM modulation waveform), where the zero sequence signal becomes zero and this calculation yields  $M_{imax[PWM]} = \frac{\pi}{2\sqrt{3}} \approx 0.907$ . With the exception of THIPWM1/4, the theoretical linearity limit of all the discussed zero sequence injection PWM methods is equal to this inverter theoretical limit. In the THIPWM1/4 method, the linearity is limited to 0.885 modulation index. However, in all these methods the inverter blanking time and minimum-pulse-width constraints imply a narrower voltage linearity range than the theoretical. Therefore, in all the discussed modulation methods, a wide overmodulation range with poor performance characteristics results.

Operating in the nonlinear modulation range, or in more common terms

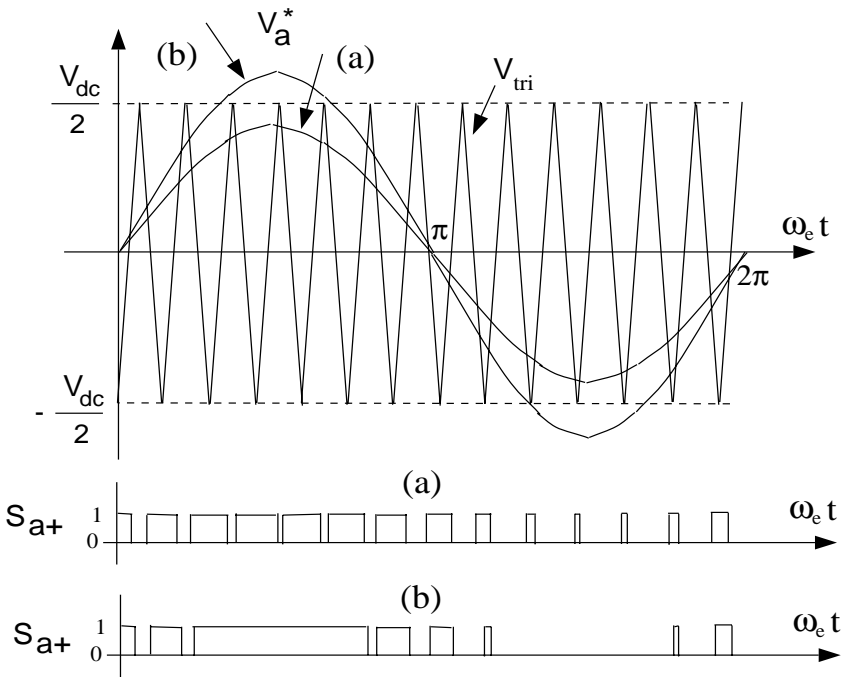


Figure 4.1: SPWM modulation waveforms and switching device gate logic signals. (a): linear modulation range, (b): overmodulation range.

the overmodulation range is problematic: large amount of subcarrier frequency harmonic voltages/currents are generated, the fundamental component voltage gain significantly decreases, and the switching device gate pulses are abruptly dropped. In  $\frac{V}{f}$  controlled PWM-VSI AC motor drives, operation in this range results in poor performance. The current ripple, and therefore, the torque ripple substantially increases. Near the six-step operating point, the harmonic current magnitude can become significantly large and frequent overcurrent fault conditions may occur. Abruptly eliminating narrow voltage pulses can induce significant transients and the poor overmodulation performance condition can be further exacerbated.

On the other hand, full inverter voltage utilization is important from cost and power density improvement perspectives. Also a drive with high overmodulation performance is less sensitive to inverter DC link voltage disturbances. In certain applications, operation in the overmodulation region may not be necessary under normal operating conditions. However, a DC link voltage sag may result an unintentional entrance to the overmodulation region. In particular, in diode rectifier front end type drives (the widemost utilized rectifier type), AC utility line voltage sag or fault conditions frequently occur and a drive operating near its rated voltage may frequently enter the overmodulation region. Under such conditions, a high performance overmodulation method could maintain the drive performance as much as possible. Hence, increased drive reliability. Therefore, the overmodulation region performance of a drive and its modulator are important and will be investigated in this chapter in detail.

With the focus being on the voltage feedforward controlled  $\frac{V}{f}$  drives, in this chapter the steady state overmodulation behavior of the modern modulators and voltage feedforward drives will be investigated. Therefore, the fundamental component voltage gain and steady state voltage/current waveform quality of the modern modulators will be analyzed in detail and performance comparison will follow. The influence of the blanking time on the modulator overmodulation range performance will be discussed. The detailed analytical and numerical investigations of modulator performance characteristics and the performance comparison will aid the overmodulation region modulator selection and design procedure. Following the establishment of high performance overmodulation algorithms, the laboratory experiments will illustrate the effectiveness of the proposed method.

## **4.2 Overmodulation Range Voltage Gain Characteristics**

In the triangle intersection technique, when the modulation wave magnitude becomes larger than the peak of the triangular wave, switching during that carrier cycle ceases, and the corresponding switch remains locked to the inverter pole within the carrier cycle. This condition is defined as the “saturation” of the particular phase. Though not commonly utilized, the terms “unmodulated phase” will be frequently utilized in this thesis to indicate the modulation signal

of the corresponding phase becomes larger than the triangular carrier wave and modulation ceases. In the beginning of the overmodulation region, depending on the modulator type, one or two of the three modulation waves are simultaneously saturated. As the modulation index increases, the saturated segments of each modulation wave and the number of simultaneously saturated phases increase according to the waveform characteristic of each modulator until the six-step operating mode is reached.

When saturation occurs, the reference per carrier cycle average voltage can not be matched by the inverter, and a voltage gain reduction results. This nonlinear voltage gain relation can be analytically modeled by Fourier analysis of the saturated modulation wave independently of the carrier frequency. Utilizing the modulation index definition, general formulas can be derived independent of the inverter voltage. However, except for the SPWM method, the voltage gain formulas of the carrier based PWM methods have not been reported, nor has a detailed gain characteristic study been conducted [52, 147, 169]. The SPWM method gain, and the gain of several other functions frequently encountered in the servomechanism systems were established many decades ago and instead of gain, the term “describing function” was utilized [52, 147]. However, the zero sequence signal injection technique, which yields functions unique to three phase systems, has not been common in control system applications. Therefore, the gain functions of zero sequence signal injection PWM methods have not been investigated until now. In the following, the gain formulas of the modern modulators are derived and a comparative evaluation follows.

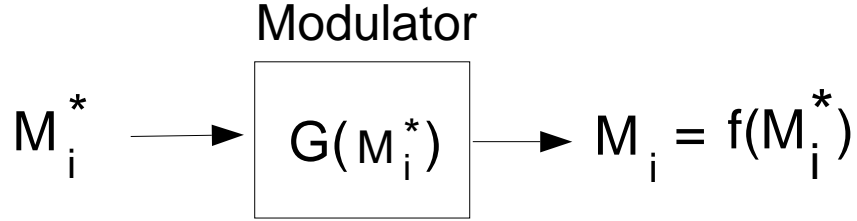


Figure 4.2: Modulation index gain block diagram of a PWM-VSI

The fundamental component voltage gain of a modulator is the ratio of the output voltage fundamental component peak value  $V_{1m}$  to the reference modulation wave fundamental component peak value  $V_m^*$ . Utilizing the modulation index and reference modulation index definitions, it can also be expressed in terms of the modulation indices as:

$$G = \frac{V_{1m}}{V_m^*} = \frac{M_i}{M_i^*} \quad (4.1)$$

The fundamental component gain formulas can be utilized in the drive overmodulation range behavior analysis, simulation, and control. With their analysis and graphic illustration, the overmodulation region behavior of the modern modulators can be studied and compared. The overmodulation region behavior of the drive can be modeled with the gain functions in computer simulations. With no PWM signals involved, the simulation can be rapid and accurate. The gain functions can also be utilized in developing a gain linearizing block for a drive controller such that proper voltage control is maintained. The the following the voltage gain functions of the modern modulators are calculated.

### 4.2.1 SPWM

As shown in Fig. 4.3, the SPWM modulation signal has quarter-wave symmetry in the overmodulation region. Utilizing this quarterwave symmetry, we calculate the fundamental component by means of Fourier analysis in the following equation.

$$V_{1m} = \frac{4}{\pi} \left( \int_0^{\alpha_s} V_m^* \sin \theta \sin \theta d\theta + \int_{\alpha_s}^{\frac{\pi}{2}} \frac{V_{dc}}{2} \sin \theta d\theta \right) \quad (4.2)$$

Writing the output voltage fundamental component in terms of the modulation index value, the following relation between the reference voltage modulation index  $M_i^*$ , and output voltage fundamental component modulation index  $M_i$  yields [169, 147, 52].

$$M_i = \left(\frac{2}{\pi}\right) M_i^* \arcsin\left(\frac{\pi}{4M_i^*}\right) + \left(\frac{1}{2}\right) \sqrt{1 - \left(\frac{\pi}{4M_i^*}\right)^2} \quad (4.3)$$

Since the output voltage fundamental component is different from the reference voltage, the output modulation index  $M_i$  has a different value from the reference modulation index  $M_i^*$ . Utilizing the definition of (4.1), the fundamental component voltage relation can be expressed by the following gain function.

$$G = \left(\frac{2}{\pi}\right) \arcsin\left(\frac{\pi}{4M_i^*}\right) + \left(\frac{1}{2M_i^*}\right) \sqrt{1 - \left(\frac{\pi}{4M_i^*}\right)^2} \quad (4.4)$$

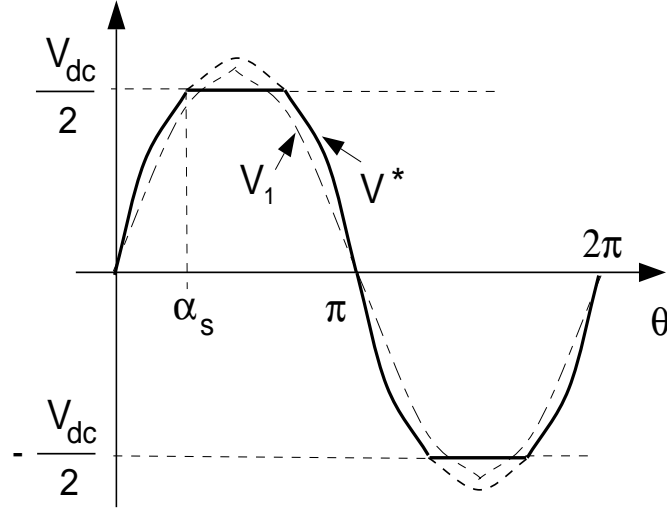


Figure 4.3: The sinusoidal PWM modulator saturation waveforms.

#### 4.2.2 SVPWM

The overmodulation range characteristics of the triangle intersection implementation of the SVPWM can be closed form modeled in the same manner as SPWM. As illustrated in Fig. 4.4, the overmodulation region consists of two sub-regions. Region I has two intersections between the saturation line and the modulation waveform per quarter wave while region II has only one intersection. Employing Fourier analysis, the fundamental component modulation index and voltage gain relations of overmodulation region I are found as follows.

$$M_i = -\frac{1}{2}M_i^* + \frac{3}{\pi}M_i^* \arcsin\left(\frac{\pi}{2\sqrt{3}M_i^*}\right) + \frac{\sqrt{3}}{2}\sqrt{1 - \left(\frac{\pi}{2\sqrt{3}M_i^*}\right)^2} \quad (4.5)$$

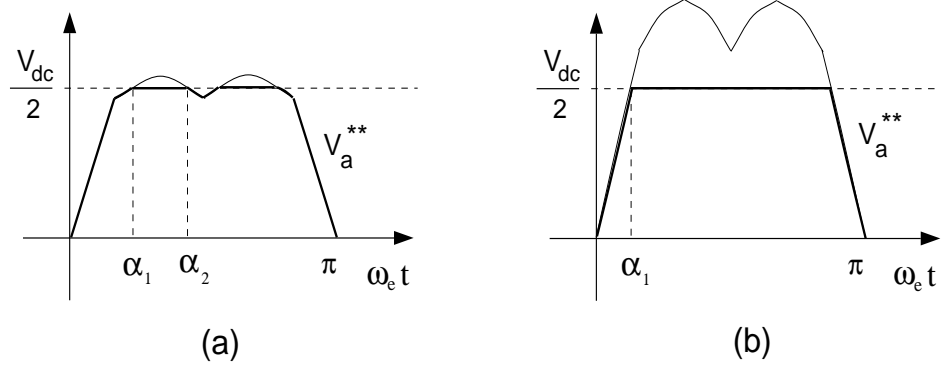


Figure 4.4: SVPWM triangle intersection method modulation waveforms in the overmodulation region. (a): Region I, (b): Region II.

$$G = -\frac{1}{2} + \frac{3}{\pi} \arcsin\left(\frac{\pi}{2\sqrt{3}M_i^*}\right) + \frac{\sqrt{3}}{2M_i^*} \sqrt{1 - \left(\frac{\pi}{2\sqrt{3}M_i^*}\right)^2} \quad (4.6)$$

Region II begins at  $M_i^* = \frac{\pi}{3} \approx 1.047$  ( $M_i \approx 0.957$ ), and the modulation index and gain relations in this region are calculated as follows.

$$M_i = \frac{3}{\pi} M_i^* \arcsin\left(\frac{\pi}{6M_i^*}\right) + \frac{1}{2} \sqrt{1 - \left(\frac{\pi}{6M_i^*}\right)^2} \quad (4.7)$$

$$G = \frac{3}{\pi} \arcsin\left(\frac{\pi}{6M_i^*}\right) + \frac{1}{2M_i^*} \sqrt{1 - \left(\frac{\pi}{6M_i^*}\right)^2} \quad (4.8)$$

### 4.2.3 THIPWM1/6

The zero sequence signal of THIPWM1/6 can be algebraically defined as  $v_0 = \frac{1}{6} V_{1m} \sin(3\omega_e t)$  [32]. This definition is based on the assumption that the associated modulation function prior to zero sequence signal injection is a sine

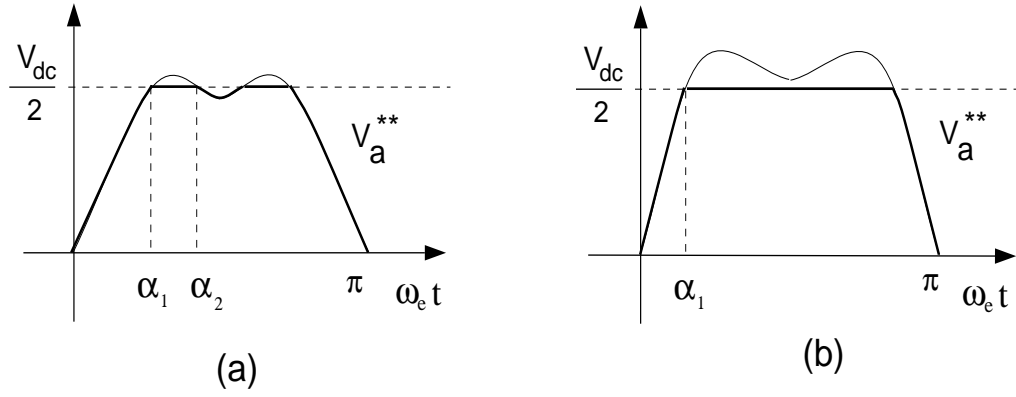


Figure 4.5: THIPWM1/6 waveforms in the overmodulation region. (a): Region I, (b): Region II.

function. The overmodulation voltage gain relations of this method are quite similar to the SVPWM methods.

As shown in Fig. 4.5 (a), in region I, the modulator waveform intersects with the saturation line twice per quarter-fundamental cycle. The intersection angles are calculated from the following transcendental equation.

$$\sin \alpha_{1,2} + \frac{1}{6} \sin 3\alpha_{1,2} = \frac{\pi}{4M_i^*} \quad (4.9)$$

The above equation can be easily solved by iterative methods. Utilizing the intersection angle values, the reference-output voltage relationship can be computed by the following formula established by the Fourier analysis of the modulation wave:

$$M_i = \left(\frac{2}{\pi}\right)M_i^* \left(\frac{\pi}{2} + \alpha_1 - \alpha_2 + \frac{5}{12}(\sin 2\alpha_2 - \sin 2\alpha_1) + \right.$$

$$\frac{1}{24}(\sin 4\alpha_2 - \sin 4\alpha_1) + \cos \alpha_1 - \cos \alpha_2 \quad (4.10)$$

The above formula is valid until the reference modulation index value of  $M_i^* = \frac{3\pi}{10} \approx 0.943$  and then region II begins. While in region II, only one intersection point exists and can be calculated from (4.9). Finally, the modulation index can be calculated from the Fourier analysis derived formula as follows.

$$M_i = \left(\frac{2}{\pi}\right)M_i^* \left(\alpha_1 - \frac{5}{12} \sin 2\alpha_1 - \frac{1}{24} \sin 4\alpha_1\right) + \cos \alpha_1 \quad (4.11)$$

Although the above formulas are dependent on the intersection angles and difficult to completely write in full closed form, they can be easily evaluated by simple numerical software packages. Once the modulation index values are calculated, the gain can be easily computed from (4.1).

#### 4.2.4 THIPWM1/4

The zero sequence signal of THIPWM1/4 can be algebraically defined as  $v_0 = \frac{1}{4}V_{1m} \sin(3w_e t)$  [32]. THIPWM1/4 loses linearity at  $M_i^* = \frac{3\sqrt{3}}{7\sqrt{7}}\pi \approx 0.885$  and its overmodulation gain characteristic can be evaluated following the same algebraic steps described in the THIPWM1/6 case.

Similar to the THIPWM1/6 case, in region I, the modulator waveform intersects with the saturation line twice per quarter-fundamental cycle. The intersection angles are calculated from the following transcendental equation.

$$\sin \alpha_{1,2} + \frac{1}{4} \sin 3\alpha_{1,2} = \frac{\pi}{4M_i^*} \quad (4.12)$$

Similar to the THIPWM1/6 case, the above equation can be easily solved by iterative methods. Utilizing the intersection angle values, the reference-output voltage relationship can be computed by the following formula established by the Fourier analysis of the modulation wave:

$$M_i = \left(\frac{2}{\pi}\right)M_i^* \left(\frac{\pi}{2} + \alpha_1 - \alpha_2 + \frac{3}{8}(\sin 2\alpha_2 - \sin 2\alpha_1) + \frac{1}{8}(\sin 4\alpha_2 - \sin 4\alpha_1)\right) + \cos \alpha_1 - \cos \alpha_2 \quad (4.13)$$

The above formula is valid until the reference modulation index value of  $M_i^* = \frac{\pi}{3} \approx 1.0472$  and then region II begins. While in region II, only one intersection point exists and can be calculated from (4.12). Finally, the modulation index can be calculated from the Fourier analysis derived formula as follows.

$$M_i = \left(\frac{2}{\pi}\right)M_i^* \left(\alpha_1 - \frac{3}{8} \sin 2\alpha_1 - \frac{1}{8} \sin 4\alpha_1\right) + \cos \alpha_1 \quad (4.14)$$

The above formulas can be computed with numerical software in a similar manner to the THIPWM1/6 case. Once the modulation index values are calculated, the gain can be easily computed from (4.1).

#### 4.2.5 DPWM1

As shown in Fig. 4.6, once in the overmodulation range, the saturated segments of DPWM1 increase beyond the  $60^\circ$  span of the linear modulation range, and the modulation wave is upward shifted by an amount dependent on the modulation index value. As shown in Fig. 4.6, the quarterwave consists of the sinusoidal portion, and beyond the point of saturation, which is indicated as  $\alpha_s$ , the reference voltage waveform consists of the constant voltage portion with the value of  $\frac{V_{dc}}{2}$ . The fundamental component voltage formula is therefore in the following.

$$V_{1m} = \frac{4}{\pi} \left( \int_0^{\alpha_s} (V_m^* (\sin \theta - \sin (\theta - \frac{2\pi}{3})) - \frac{V_{dc}}{2}) \sin \theta d\theta + \int_{\alpha_s}^{\frac{\pi}{2}} \frac{V_{dc}}{2} \sin \theta d\theta \right) \quad (4.15)$$

Fourier analysis of the saturated wave yields the following modulation index and voltage gain relations.

$$M_i = -1 + \left( \frac{\sqrt{3}}{\pi} - \frac{1}{2} \right) M_i^* + \left( \frac{\pi}{4\sqrt{3}} \right) \frac{1}{M_i^*} + \left( \frac{3}{\pi} \right) M_i^* \arcsin \left( \frac{\pi}{2\sqrt{3}M_i^*} \right) + \left( \frac{\sqrt{3}}{2} \right) \sqrt{1 - \left( \frac{\pi}{2\sqrt{3}M_i^*} \right)^2} \quad (4.16)$$

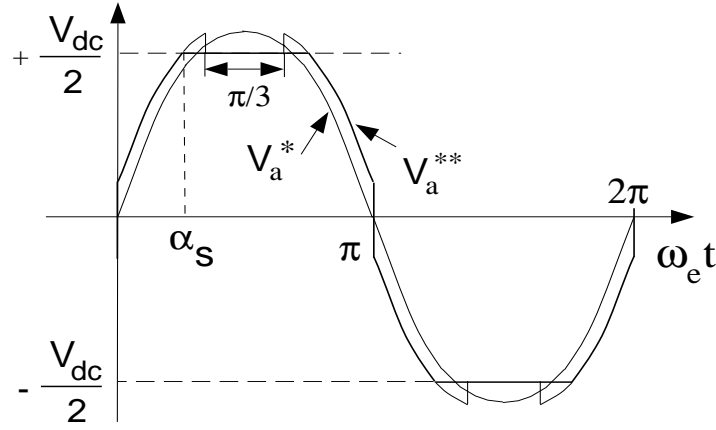


Figure 4.6: DPWM1 method overmodulation waveforms.

$$G = \frac{-1}{M_i^*} + \left(\frac{\sqrt{3}}{\pi} - \frac{1}{2}\right) + \left(\frac{\pi}{4\sqrt{3}}\right)\frac{1}{M_i^{*2}} + \left(\frac{3}{\pi}\right)\arcsin\left(\frac{\pi}{2\sqrt{3}M_i^*}\right) + \left(\frac{\sqrt{3}}{2M_i^*}\right)\sqrt{1 - \left(\frac{\pi}{2\sqrt{3}M_i^*}\right)^2} \quad (4.17)$$

#### 4.2.6 DPWM2 and DPWM0

The DPWM2 modulation wave is not quarter-wave symmetric, hence the overmodulation voltage gain equations are complex compared to the previous cases.

As shown in Fig. 4.7, the overmodulation region is divided into two subregions. In the first subregion, as shown in Fig. 4.7 (a), the modulation wave has four saturated segments per fundamental cycle. Employing Fourier analysis and utilizing the intermediate variables  $\psi$ ,  $a_1$ , and  $b_1$ , the voltage relations in the first region can be calculated from the following equations.

$$\psi = -\frac{\pi}{3} + \arcsin\left(\frac{\pi}{2\sqrt{3}M_i^*}\right) \quad (4.18)$$

$$a_1 = \frac{M_i^*}{4} - \frac{\sqrt{3}}{2} \sin\left(\psi - \frac{\pi}{6}\right) + \frac{3\psi}{2\pi} M_i^* - \frac{3}{4\pi} M_i^* \cos\left(2\psi + \frac{\pi}{6}\right) \quad (4.19)$$

$$b_1 = -\frac{1}{2} \cos\left(\psi + \frac{\pi}{3}\right) + \frac{\sqrt{3}}{4\pi} M_i^* \left(\frac{\pi}{3} - 2\psi - \sin\left(2\psi - \frac{\pi}{3}\right)\right) \quad (4.20)$$

$$M_i = \sqrt{a_1^2 + b_1^2} \quad (4.21)$$

The second subregion begins at  $M_i^* = \frac{\pi}{3}$ . Shown in Fig. 4.7 (b) the modulation wave heavily saturates and on each side two saturated segments merge, leading to only two saturated segments per cycle. Introducing the variable  $\alpha$ , the coefficients  $a_1$ , and  $b_1$  can be calculated as follows.

$$\alpha = \frac{2\pi}{3} - \arcsin\left(\frac{\pi}{2\sqrt{3}M_i^*}\right) \quad (4.22)$$

$$a_1 = \frac{\sin \alpha}{2} + \left(\frac{1}{2} - \frac{\sqrt{3}}{8\pi} - \frac{3}{4\pi}\alpha\right) M_i^* - \frac{\sqrt{3}}{4\pi} M_i^* \cos\left(2\alpha - \frac{2\pi}{3}\right) \quad (4.23)$$

$$b_1 = -\frac{\cos \alpha}{2} + \frac{\sqrt{3}}{2\pi} M_i^* \left(\frac{\sqrt{3}}{4} - \frac{1}{2} \sin\left(2\alpha - \frac{2\pi}{3}\right) + \frac{\pi}{3} - \frac{\alpha}{2}\right) \quad (4.24)$$

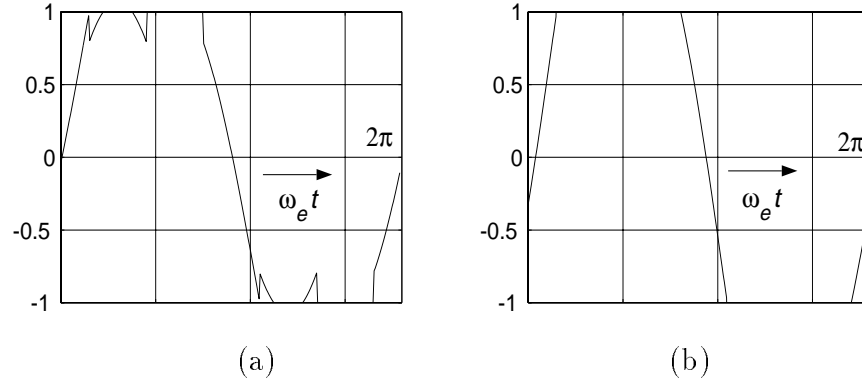


Figure 4.7: DPWM2 overmodulation waveforms. (a): Region I, (b): Region II.

Once the above coefficients are known, the reference-output voltage relations can be calculated from (4.21) and the voltage gain can be calculated in both subregions from the definition of (4.1).

The modulation waves of DPWM2 and DPWM0 are only different by the position of the unmodulated segment. Therefore, Fourier analysis of both yield the same fundamental component gain results. For this reason the derivation for DPWM0 will not be pursued and the above results can be readily utilized when necessary.

### 4.2.7 DPWM3

As shown in Fig. 4.8, the overmodulation region of DPWM3 is divided into three subregions. The first subregion covers the reference modulation index range of  $\frac{\pi}{2\sqrt{3}} \leq M_i^* \leq \frac{\pi}{3}$ . In this region the modulation index relations are calculated in the following.

$$M_i = 1 + \left(1 - \frac{\sqrt{3}}{\pi}\right)M_i^* - \frac{\pi}{4\sqrt{3}M_i^*} - \frac{3}{\pi}M_i^* \arccos\left(\frac{\pi}{2\sqrt{3}M_i^*}\right) + \frac{\sqrt{3}}{2} \sqrt{1 - \left(\frac{\pi}{2\sqrt{3}M_i^*}\right)^2} \quad (4.25)$$

The second subregion covers the range of  $\frac{\pi}{3} \leq M_i^* \leq \frac{\pi}{\sqrt{3}}$  and the modulation index formula of this region is as follows.

$$M_i = 1 + \left(\frac{1}{2} - \frac{\sqrt{3}}{\pi}\right)M_i^* \quad (4.26)$$

The third and last region covers the range of  $\frac{\pi}{\sqrt{3}} \leq M_i^* \leq \infty$  and in this region the following modulation index relations are valid.

$$M_i = -1 + 2\cos\beta + \left(\frac{1}{2} - \frac{3\beta}{\pi} - \frac{\sqrt{3}}{2\pi}\right)M_i^* + \frac{\sqrt{3}}{\pi}M_i^* \sin\left(2\beta - \frac{\pi}{6}\right) \quad (4.27)$$

$$\beta = \frac{\pi}{6} - \arcsin\left(\frac{\pi}{2\sqrt{3}M_i^*}\right) \quad (4.28)$$

Evaluating the above formula for  $M_i^* \rightarrow \infty$  the modulation index of  $M_i = \sqrt{3} - 1 \approx 0.732$  is found. This result indicates DPWM3 has an unusual over-modulation behavior. In the third region, as the reference modulation index increases, the fundamental component signal magnitude decreases. Unlike all the other modulators, which experience saturation, this modulator generates a reduced output voltage and exacerbates the drive performance.

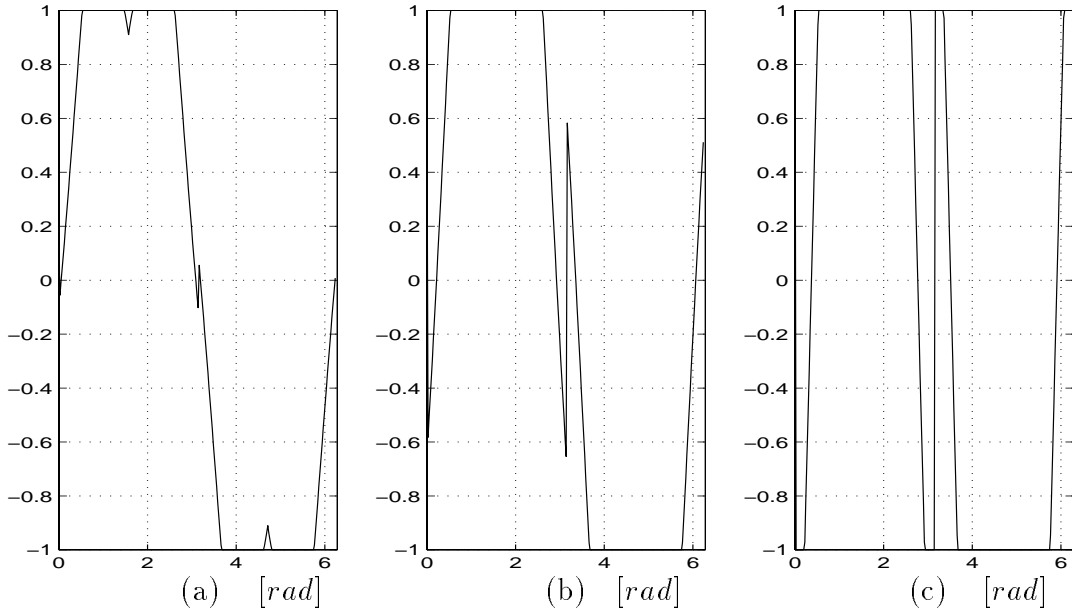


Figure 4.8: DPWM3 method overmodulation waveforms for three  $M_i^*$  values. (a): Region I ( $M_i^* = 1.0$ ), (b): Region II ( $M_i^* = 1.5$ ), (c): Region III ( $M_i^* = 3.0$ ).

As illustrated in Fig. 4.8(c), in the third overmodulation region, this modulator generates voltage pulses with opposite polarity to the fundamental component, therefore the output voltage becomes smaller. As the reference signal becomes large, the opposite polarity pulses become rectangles with  $30^\circ$  width.

#### 4.2.8 GDPWM

Since GDPWM covers the DPWM0, DPWM1 and DPWM2 modulators, its fundamental component overmodulation gain model has been developed in the previous subsections at least for these operating points. The following sections will illustrate except for these operating points, the remaining  $\psi$  range

of GDPWM does not have practical importance from the overmodulation perspective. Since a generalized fundamental component gain formula of GDPWM would be substantially complex and it has no practical value, its derivation will not be pursued in this work.

#### **4.2.9 DPWMMAX and DPWMMIN**

Since these modulators have a zero sequence signal with DC bias, in the overmodulation region, the output voltage contains a DC average voltage output. Therefore, the overmodulation region operation of these modulators is prohibitive and their waveform analysis will not be pursued in this work.

### **4.3 On The Gain Formula Accuracy**

Obvious from the above analyses, the gain function calculation involves continuous or piece-wise continuous modulation signals, as opposed to the actual PWM inverter output voltages consisting of high frequency rectangular pulses. Theoretically, a modulator could match the reference volt-seconds within every carrier cycle and as a result the per-carrier-cycle-average-voltage could approach the theoretical modulation signals. Therefore, high fundamental component voltage gain accuracy is expected. However, at least in the regularly sampled asynchronous PWM, the discretized modulation signal may yield a slightly different volt-seconds than the original signal due to finite sampling

rate. Therefore, the theoretical gain formula can yield a slightly different fundamental component than the actual.

To test the accuracy of the Fourier analysis based fundamental component gain calculation method, the SVPWM method (the choice of SVPWM modulator was arbitrary) gain calculation was compared with simulation data. Employing the regularly sampled SVPWM modulator, an ideal PWM-VSI simulation was utilized to generate the pulsating inverter output voltage data. Evaluating the simulation data with a Fast Fourier Transformation (FFT) program, the fundamental component signal could be computed with high accuracy ( $2^{13} = 8192$  data points). The fundamental frequency was selected as 50 Hz and the carrier frequency was varied from 1 to 5 kHz to investigate the influence of the sampling rate. The results are illustrated in Table 4.1 in terms of modulation indices. Based on the table data, the relative error was calculated for all the data and it was found to be less than 0.5 % and higher carrier frequencies implied significantly better accuracy.

The above results indicate for  $\frac{f_s}{f_e} > 20$ , the relative gain error is less than 0.5 % and the error significantly decreases with increasing  $\frac{f_s}{f_e}$ . Since the widely utilized PWM-VSI drives employing Insulated Gate Bipolar Transistor (IGBT) devices typically have high  $\frac{f_s}{f_e}$  values, the model successfully represents most inverter drives.

Table 4.1: SVPWM theoretical and simulation based  $M_i = f(M_i^*)$  data

$M_i^*$	$M_i^t$	$M_i(5kHz)$	$M_i(2kHz)$	$M_i(1kHz)$
0.907	0.907	0.907	0.907	0.907
0.950	0.934	0.934	0.933	0.933
1.0	0.949	0.949	0.948	0.946
2.0	0.989	0.988	0.987	0.984
4.0	0.997	0.997	0.996	0.993

## 4.4 Voltage Gain Comparisons

In this section the voltage gain characteristics of all the discussed modulators are comparatively evaluated. The comparisons are provided in terms of the voltage gain ( $G = f(M_i)$ ) and modulation index ( $M_i = f(M_i^*)$ ) relations. Utilizing the gain functions derived in the previous section, the gain characteristics of the modern modulators are computed and illustrated in Fig. 4.9. The improvement in the linearity range of all the zero sequence injection methods compared to SPWM is obvious from the figure. More importantly, the graph reveals the superior gain characteristic of Depenbrock's DPWM1 method; the gain of this modulator drops at a significantly smaller rate than all the other modulators, and the minimum value, which occurs at the six-step operating point is  $\frac{\sqrt{3}}{\pi} \approx 0.551$ . All the other modulators have a rapid drop in gain and eventually the gain becomes practically zero at the six-step operating point. With the exception of DPWM3, the similarity of their gain characteristics with respect to each other is also obvious from the figure.

With its most unusual and poorest gain characteristic, the DPWM3 method would perhaps be mainly of academic interest. Unlike all the other modulators, which experience saturation, this modulator generates a substantially reduced output voltage and exacerbates the drive performance. Since in the overmodulation region the voltage pulse pattern of this modulator does contradict the pulse polarity consistency principle, its performance is unacceptable. In particular, its application to closed loop speed regulated voltage feedforward drives is prohibitive. Therefore, no further investigation on this modulator has been attempted.

Shown in Fig. 4.10 and illustrated in terms of the modulation indices, the input-output voltage relations of the important modulators provide more specific information. Except for DPWM1, all the modulators require large reference signals in order to penetrate the overmodulation region. In particular, DPWM1 requires a reference signal with a magnitude of  $M_i^* = \frac{\pi}{\sqrt{3}} \approx 1.81$ , while the other modulators require signals with very large magnitudes ( $M_i^* \approx 5...20$ ). This result is extremely important from an implementation perspective: the smaller the gain range, the better the accuracy of the modulation signal and the smaller word length requirement of a signal processor (or the signal range in an analog implementation). Therefore, DPWM1 utilizes the signal range of a processor with high resolution and abrupt pulse dropping and the consequent overcurrent fault condition is avoided.

The unusual gain characteristic of DPWM1 is not difficult to explain. In the

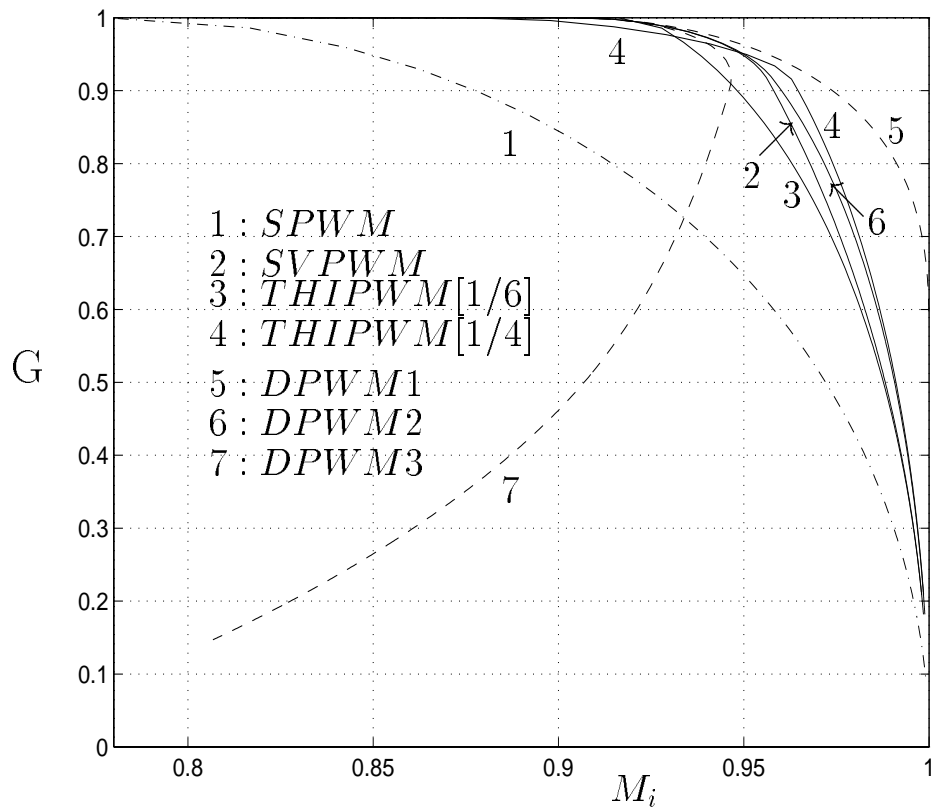


Figure 4.9:  $G = f(M_i)$  voltage gain characteristics of the popular modulators.

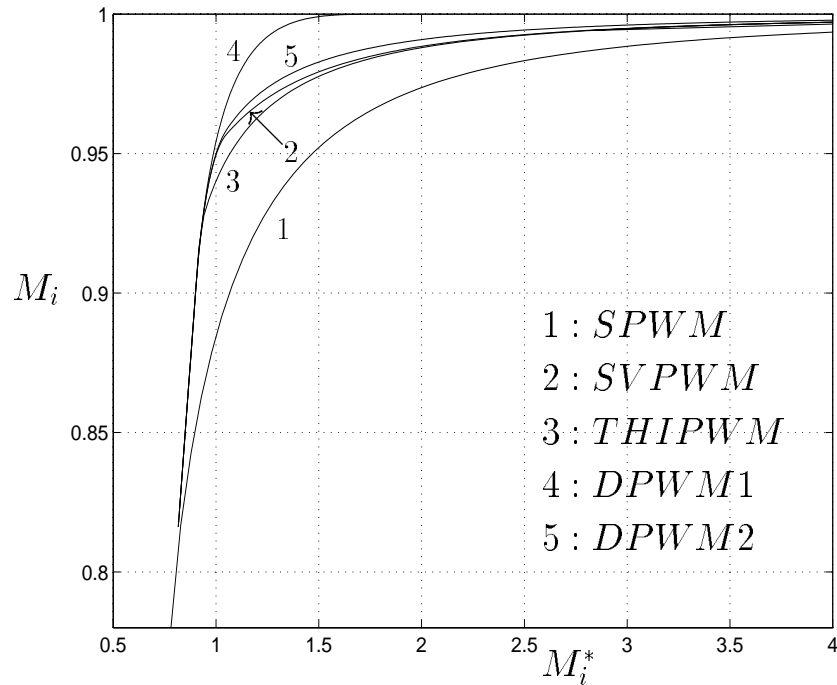


Figure 4.10: Overmodulation region  $M_i = f(M_i^*)$  characteristics.

overmodulation range, the zero sequence signal of this modulator is effectively a square-wave function with an increasing magnitude as the six-step operating point is approached. Therefore, in this method, the modulation wave is vertically and horizontally forced to approach the six-step mode, while the other zero sequence injection methods force the modulation wave to expand mainly horizontally until the six-step mode is generated. This characteristic of DPWM1 can be clearly observed in Fig. 4.11 where DPWM1 and SVPWM modulation waveforms are compared for a set of reference modulation index values. It is apparent that as the reference modulation index increases, the SVPWM modulation wave saturates heavily, while the DPWM1 modulation wave easily approaches the square-wave.

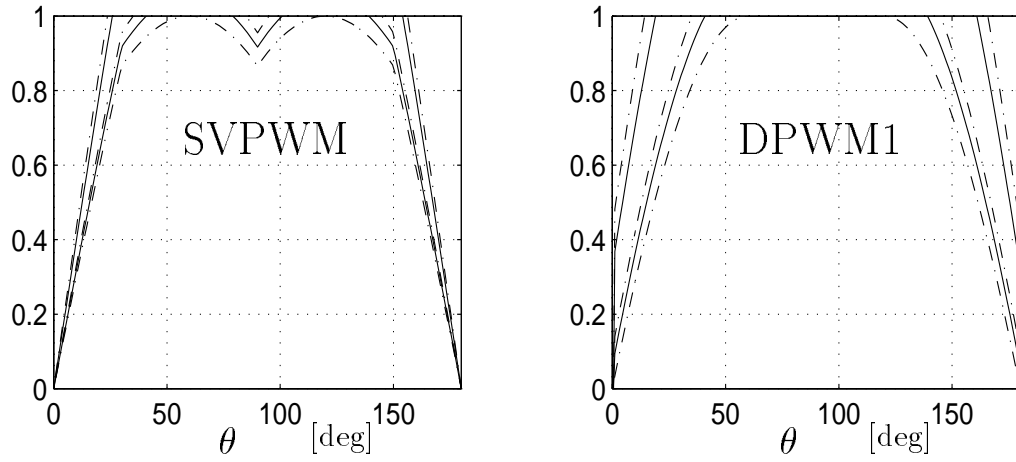


Figure 4.11: Overmodulation region modulation wave profiles of SVPWM and DPWM1 for five different  $M_i^*$  values.

## 4.5 Influence Of Blanking Time And Minimum Pulse Width On Modulator Gain

The inverter voltage linearity section of the previous chapter provided a short introduction to the influence of the inverter non-ideal characteristics (such as the minimum pulse width and the inverter blanking time) on the modulator voltage gain behavior. This section provides a more detailed investigation of these characteristics.

Inverter blanking time is the time interval that both switches of an inverter leg are open following a change in the gate logic reference signal value. It is provided for protection against DC bus short circuit. As shown in Fig. 4.12(b), the blanking time controller delays the reference gate signals by the blanking time  $t_d$ , and results in loss of gate signal symmetry (increases the uncharacteristic

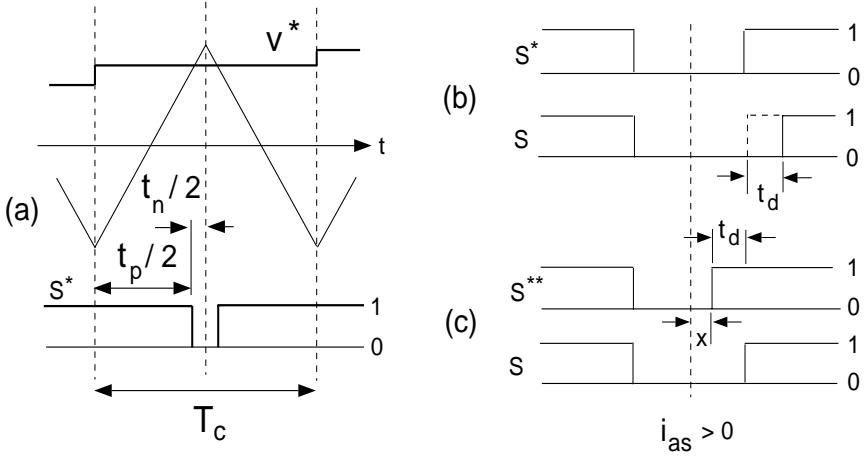


Figure 4.12: Regular sampling PWM reference and gate signals. (a): The reference gate signal at high modulation level, (b): No compensation results in asymmetric gate signal ( for  $i_{as} > 0$ ), (c): Signal after exact compensation.

harmonics), and also a reduction in the output voltage value. Typically, a gate pulse correction (compensation) algorithm is employed in order to restore the symmetry and volt-second balance [117]. As shown in Fig. 4.12 (c), in the exact compensation method, if the polarity of the phase current of the corresponding inverter leg is positive (negative), the reference gate signal on the triangle side with negative(positive) slope is advanced (delayed) by the blanking time leading to the correct output voltage pulse.

When a modulator operates near its theoretical linearity limits, as shown in Fig. 4.12 (a), narrow gate pulses are generated. When the width of such pulses becomes smaller than  $2t_d$  ( $t_d$  is the blanking time), the compensation algorithm fails to correct the pulses properly. In Fig. 4.12 (c), this condition corresponds to  $x \leq 0$  and correct compensation requires interference with the

modulation signal in the previous half carrier cycle. Since in the conventional digital PWM methods the reference modulation signal is generated only at the positive and/or negative peak points of the triangular carrier wave (regular sampling), correct compensation of such a narrow pulse is not possible. Hence, voltage gain reduction occurs before the theoretical linearity limit. The lowest modulation level at which this problem occurs can be easily calculated. When the modulation signal  $v^*$  is positive, the narrow pulse occurs when in the upper inverter leg switch is the off state with a duration  $t_n^*$  calculated as follows.

$$t_n^* = \left(\frac{T_s}{2}\right)\left(1 - \frac{v^*}{\frac{V_{dc}}{2}}\right) \quad (4.29)$$

Substituting the modulation wave peak value of the modulator under investigation in the above formula and selecting the minimum pulse width equal to  $2t_d$ , the practical maximum linear modulation index  $M_{Lmax}^p$  can be found as follows.

$$M_{Lmax}^p = \left(1 - k_m \frac{2t_d}{T_s}\right) * M_{Lmax}^t \quad (4.30)$$

In the above formula,  $M_{Lmax}^t$  is the theoretical linearity limit of the modulator. The  $k_m$  coefficient distinguishes the discontinuous PWM methods from the continuous wave modulation methods. Its value is  $k_m = 1$  for the DPWM methods and  $k_m = 2$  for the modulators with continuous modulation wave. Note the above equation and (3.54) are derived with the same approach and replacing

$2t_d$  with  $t_{MPW}$  yields equal results. As discussed in the previous chapter, the small  $k_m$  coefficient of the DPWM methods indicates that DPWM methods have wider voltage linearity range than SPWM, SVPWM, and other CPWM methods. This result is a consequence of the different distribution of the inverter zero states in the two different modulation groups. The discontinuous PWM methods generate only one inverter zero state per carrier cycle ( $t_0$ : all the lower inverter switches are in the on-state or  $t_7$ : all the upper switches are in the on-state), while the continuous PWM methods generate two zero states (for SVPWM  $t_0 = t_7$ ). Since the total zero state time is not a function of the zero sequence signal but the line-line reference voltage, for the same line-line output voltage and carrier frequency value, the gate pulses of the DPWM methods are wider than the gate pulses of the CPWM methods. Therefore, the narrow pulse problem occurs at a higher modulation index with DPWM methods than CPWM methods.

Notice that in both continuous and discontinuous PWM cases, the linearity boundaries depend on the ratio of the blanking time to the carrier cycle. Since the increasing carrier cycle practically implies increasing inverter power and increasing blanking time, the ratio is at least a few percent in most PWM-VSI drives. As a result, in most applications the linearity range of a modulator is reduced by a substantial amount. In either modulation method, once beyond the boundary of linear modulation range, the output voltage is reduced by an amount which depends on the overlap time “x” shown in Fig. 4.12 (c). As a result, the gain begins to decrease at a lower modulation index than the

theoretical linearity limit and decreases more rapidly than the theoretical gain characteristic. Compared to the modulator theoretical gain reduction, the gain reduction of the DPWM methods due to the blanking time is fairly small, and can be ignored for inverters with a few kHz switching frequency and blanking time less than a few microseconds. In the Gate Turn Off (GTO) switching device based PWM-VSI applications, the effect is more emphasized due to the long blanking time.

In certain applications, the narrow voltage pulses which occur at high modulation levels may damage the drive or load. In such cases the blanking time correction algorithm yields to a Minimum Pulse Width (MPW) control algorithm. For example, the turn-on and/or turn-off speed capabilities of a GTO may not be sufficient to generate such narrow pulses. In order to avoid commutation failure of GTO based drives, such narrow pulses are either eliminated or fixed at an acceptable level.

Narrow voltage pulses can also cause overvoltage related motor insulation failure. State of the art PWM-VSI drives utilize the modern third generation IGBT devices with very small turn-on and turn-off times. Feeding motors with long cables from such PWM-VSI drives, significant overvoltages are generated across the motor terminals due to voltage reflection. As a result, the motor terminals experience excessive overvoltages contributing to insulation failure. When such PWM-VSI drives operate at high modulation levels and narrow

pulses are generated, the voltage reflection problem is exacerbated: overvoltages in excess of twice the DC bus value can appear across the terminals of a motor connected to a drive through as short a cable as 30 m [92]. Therefore, narrow voltage pulses are problematic in many drives. These problems can be eliminated by either employing passive solutions such as inserting reactors between the drive and the motor, or active solutions such as MPW control which only requires modification to the PWM algorithm of a drive. The active solution is more economic, compact and maintenance free.

When employed, MPW control algorithms affect the modulator voltage gain and reduce the linear modulation range noticeably. The Pulse Elimination Method (PEM) omits pulses narrower than a desirable limit and increases the modulator gain. The Pulse Limiting Method (PLM) limits the width of the pulses to the minimum allowable pulse width limit and reduces the gain. However, as the modulation index increases, the modulator theoretical gain characteristics dominate and in both cases the gain decreases rapidly, therefore the gain curves follow the gain curves of Fig. 4.9 closely. In either method, the linearity limit of a modulator becomes smaller than the theoretical limits. In a proper design, the MPW pulses are wider than  $2t_d$ ; therefore, the blanking time controller has no influence on the modulator linearity in this case. When MPW is applied, the practical voltage linearity limit of an inverter can be found from (3.54). Since in this algorithm both sides of the triangle are affected while in the blanking time compensation case only one side of the triangle has incorrect

gate signal, the effect of MPW control has more influence on the gain characteristic of a PWM-VSI. In particular, in GTO based high power PWM-VSIs which employ GTO's with large MPW values ( $t_{MPW} \approx 200\mu s$ ), MPW control starts at very low modulation depths, and the nonlinear gain characteristics dominate the drive behavior at a low modulation depth. Although less significant, the effect can not be underemphasized in the modern IGBT device based PWM-VSI drives. In order to avoid the above mentioned overvoltage problem, MPW times as large as 8-16  $\mu s$  are required [92]. Since the carrier frequency is at least a few kilohertz, the influence of MPW control on the gain characteristics of such drives is significant.

The MPW controlled modulator gain formulas can be closed form calculated by modifying the theoretical modulator gain formulas. In a PEM controlled inverter, the output modulation index is different from the modulation index output by an amount the additional volt-seconds determine. Calculating the additional components by the Fourier analysis, the modified modulation index relations can be easily obtained. In the following the modified modulation index formulas of SPWM, SVPWM, and DPWM1 are summarized.

#### 4.5.1 SPWM

When employing PEM, the modulation index relations of the SPWM method become as follows.

$$M'_{iSPWM} = M_i + \cos \alpha_{0s} - \cos \alpha_{1s} - \frac{2M_i^*}{\pi} \left[ \alpha_{1s} - \alpha_{0s} - \frac{1}{2} (\sin (2\alpha_{1s}) - \sin (2\alpha_{0s})) \right] \quad (4.31)$$

The  $\alpha_{0s}$  and  $\alpha_{1s}$  angles correspond to points PEM begins and ends. These angles are calculated as follows.

$$\alpha_{0s} = \arcsin \left( \frac{\pi}{4M_i^*} \left( 1 - \frac{2t_{MPW}}{T_s} \right) \right) \quad (4.32)$$

$$\alpha_{1s} = \arcsin \left( \frac{\pi}{4M_i^*} \right) \quad (4.33)$$

## 4.5.2 SVPWM

The SVPWM modulation index relations with PEM control are calculated in the following for three operating regions. In the first region, for  $\frac{\pi}{2\sqrt{3}} \left( 1 - 2\frac{t_{MPW}}{T_s} \right) \leq M_i^* \leq \frac{\pi}{2\sqrt{3}}$  the following relations yield.

$$M'_{iSVPWM} = M_i^* + \cos \alpha_{1sv1} - \cos \left( \frac{2\pi}{3} - \alpha_{1sv1} \right) - \frac{\sqrt{3}M_i^*}{2\pi} \left[ \sqrt{3} \left( \frac{2\pi}{3} - 2\alpha_{1sv1} \right) + \sin \left( 2\alpha_{1sv1} + \frac{\pi}{6} \right) + \cos (2\alpha_{1sv1}) \right] \quad (4.34)$$

$$\alpha_{1sv1} = -\frac{\pi}{6} + \arcsin \left( \frac{\pi}{2\sqrt{3}M_i^*} \left( 1 - \frac{2t_{MPW}}{T_s} \right) \right) \quad (4.35)$$

The second region involves a reference modulation index range of  $\frac{\pi}{2\sqrt{3}} \leq M_i^* \leq \frac{\pi}{3}$  and in this region the modulation index relations are as follows.

$$M'_{iSVPWM} = M_i + \cos \alpha_{1sv2} + \cos \alpha_{3sv2} - \cos \alpha_{2sv2} - \cos \alpha_{4sv2} + \frac{3M_i^*}{2\pi} (\alpha_{1sv2} + \alpha_{3sv2} - \cos \alpha_{2sv2} - \cos \alpha_{4sv2}) + \frac{\sqrt{3}M_i^*}{2\pi} [\sin(2\alpha_{2sv2} + \frac{\pi}{6}) + \sin(2\alpha_{4sv2} + \frac{\pi}{6}) - \sin(2\alpha_{1sv2} + \frac{\pi}{6}) - \sin(2\alpha_{3sv2} + \frac{\pi}{6})] \quad (4.36)$$

$$\alpha_{1sv2} = -\frac{\pi}{6} + \arcsin\left(\frac{\pi}{2\sqrt{3}M_i^*} \left(1 - \frac{2t_{MPW}}{T_s}\right)\right) \quad (4.37)$$

$$\alpha_{2sv2} = -\frac{\pi}{6} + \arcsin\left(\frac{\pi}{2\sqrt{3}M_i^*}\right) \quad (4.38)$$

$$\alpha_{3sv2} = \frac{2\pi}{3} - \alpha_{2sv2} \quad (4.39)$$

$$\alpha_{4sv2} = \frac{2\pi}{3} - \alpha_{1sv2} \quad (4.40)$$

The third region involves the remainder of the reference modulation index range ( $M_i^* \geq \frac{\pi}{3}$ ) and in this region the modulation index relations are as follows.

$$M'_{iSVPWM1} = M_i + \cos \alpha_{0sv3} - \cos \alpha_{1sv3} - \frac{3M_i^*}{\pi} [\alpha_{1sv3} - \alpha_{0sv3} - \frac{1}{2}(\sin(2\alpha_{1sv3}) - \sin(2\alpha_{0sv3}))] \quad (4.41)$$

$$\alpha_{0sv3} = \arcsin\left(\frac{\pi}{6M_i^*}\left(1 - \frac{2t_{MPW}}{T_s}\right)\right) \quad (4.42)$$

$$\alpha_{1sv3} = \arcsin\left(\frac{\pi}{6M_i^*}\right) \quad (4.43)$$

### 4.5.3 DPWM1

When employing PEM, the modulation index relations of the DPWM1 method become as follows.

$$\begin{aligned} M'_{iDPWM1} = M_i + 2(\cos \alpha_{d0} - \cos \alpha_{d1}) - M_i^* \frac{3}{\pi}(\alpha_{d1} - \alpha_{d0}) + \\ M_i^* \frac{\sqrt{3}}{\pi}(\sin(2\alpha_{d1} + \frac{\pi}{6}) - \sin(2\alpha_{d0} + \frac{\pi}{6})) \end{aligned} \quad (4.44)$$

In the above equation,  $M'_i$  is the output voltage modulation index and  $M_i$  is the theoretical modulation index value without MPW control which is given by (4.16). The intermediate variables  $\alpha_{d0}$  and  $\alpha_{d1}$  are calculated as follows.

$$\alpha_{d0} = -\frac{\pi}{6} + \arcsin\left(\frac{\pi}{2\sqrt{3}M_i^*}\left(1 - \frac{t_{MPW}}{T_s}\right)\right) \quad (4.45)$$

$$\alpha_{d1} = -\frac{\pi}{6} + \arcsin\left(\frac{\pi}{2\sqrt{3}M_i^*}\right) \quad (4.46)$$

#### 4.5.4 Evaluation and Comparison

Figure 4.13 shows the closed form calculated gain characteristics of PEM controlled PWM-VSI for both SVPWM and DPWM1. Both modulators employ  $f_s = 5kHz$  and  $t_{MPW} = 12\mu s$ . As the figure illustrates, the influence of the MPW algorithm has a non-negligible effect on the voltage gain of SVPWM. The nonlinearity is noticeably smaller in the DPWM1 case. On the same figure, the blanking time dependent gain characteristic of DPWM1 is shown for  $t_d = 4\mu s$ . Notice the blanking time has very little influence on the linearity compared to MPW. The gain curves of the PEM controlled drive clearly indicate the linearity range of DPWM methods is significantly wider than SVPWM and in the overmodulation region DPWM1 is the only modulator that maintains a high gain. Therefore, DPWM1 can be most beneficial to high power PWM-VSI drives and all the PWM-VSI drives with large  $\frac{t_{MPW}}{T_s}$  ratio while operating in the high modulation range.

### 4.6 Voltage Gain Linearization

As illustrated in Fig. 4.14 (a) in block diagram form, in the overmodulation region the VSI output voltage is different from the reference voltage due to gain nonlinearity. PWM-VSI drives which employ PLM and drives which do not employ any MPW control algorithm always experience gain reduction, while those employing PEM experience gain increase in the entrance of the overmodulation

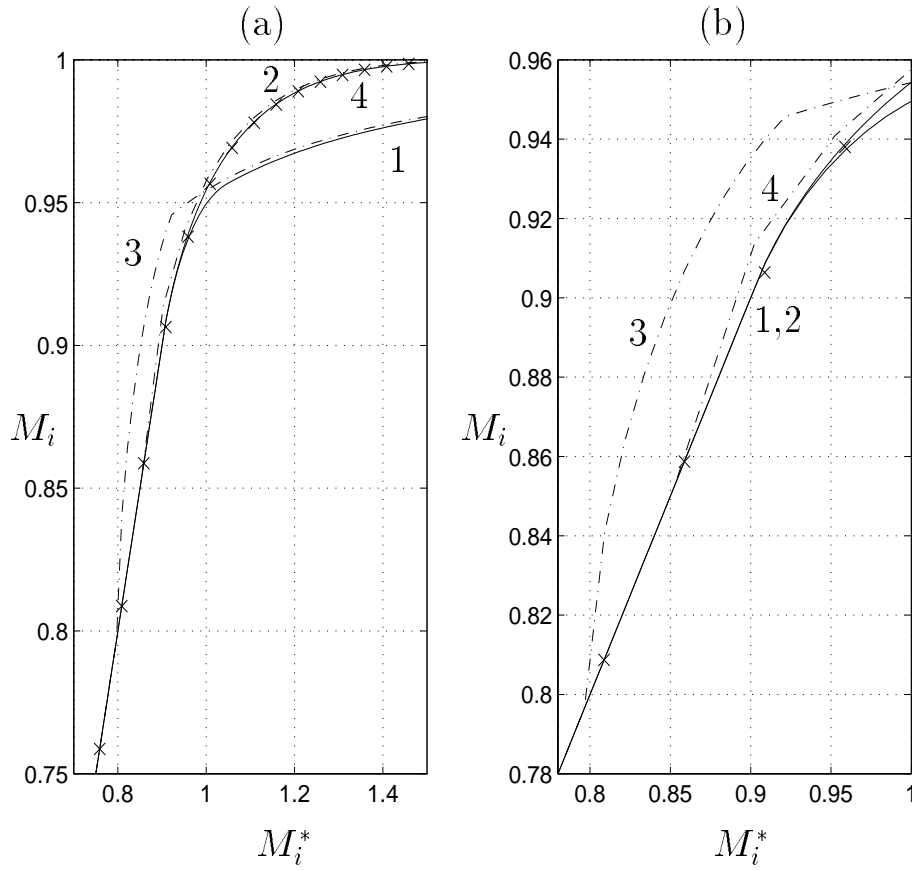


Figure 4.13: SVPWM and DPWM1 theoretical  $M_i = f(M_i^*)$  characteristics (a), and the magnified view in the low end of the overmodulation region (b). 1: SVPWM, 2: DPWM1, 3: SVPWM with MPW, and 4: DPWM1 with MPW. The blanking time dependent nonlinearity of DPWM1 is shown with the “×” symbol.

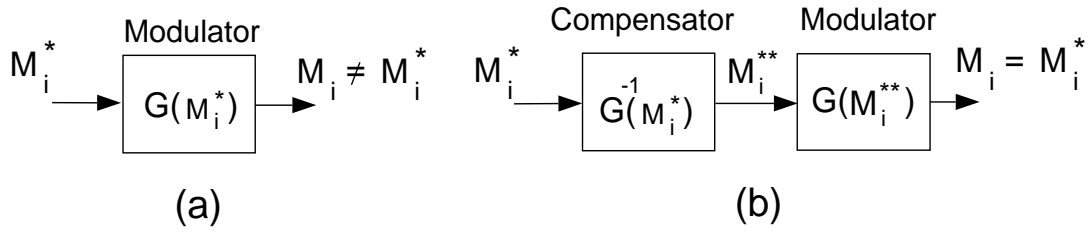


Figure 4.14: Overmodulation range voltage gain block diagrams. (a): Modulator nonlinear gain characteristic. (b): The compensator cancels the nonlinearity by inverse gain multiplication.

region and gain reduction as the overmodulation region is further penetrated. On the other hand, it is important to program the reference fundamental component voltage value correctly so that the drive performance does not degrade. For example, in AC motor drive applications the stator flux value (or equivalently the  $\frac{V}{f}$  value) must be maintained at a proper level to obtain high efficiency. Therefore, fundamental component voltage linearity must be retained in the overmodulation range also. Since the discussed modulation methods have nonlinear gain characteristics, to retain voltage linearity a gain compensation technique must be employed. Gain compensation techniques are based on either adding extra signals such as square-waves to the reference modulation waves, or by increasing or decreasing the fundamental component magnitude of the reference modulation waves [93]. As shown in Fig. 4.14 (b), in the latter approach the reference modulation wave fundamental component signal is pre-multiplied with the inverse gain function such that the nonlinearity is canceled. The former approach may alter the modulator harmonic characteristics while the latter does not. In this work, the inverse gain method will be investigated.

In both gain linearization methods, calculating the gain compensation function is very difficult. The difficulty of describing the gain functions in closed form equations has been overcome in the early stages of this paper. However, closed form calculation of the inverse gain function is very difficult. Furthermore, on-line computation of such complex gain compensation signals with the state of the art DSP or  $\mu P$  devices is prohibitive. Instead, the gain function and its inverse can be numerically computed off-line and the data can be utilized to approximate the gain compensation function by a look-up table and/or a simple curve fitting method.

Inverse gain compensation based gain linearization of the SPWM method which employs a table look-up approach was previously reported, and the requirement for a large table size and an efficient table search algorithm were indicated [93]. The zero sequence injection PWM methods which are discussed in this paper have smaller gain range than SPWM, therefore the memory requirements are less demanding. However, of all the discussed methods, DPWM1 provides an exceptional implementation advantage due to its significantly small gain reduction. The gain compensation signal (inverse gain function magnitude) of DPWM1 is less than 2 units while the other modulators require large signals ranging from 5 to 20 units. Therefore, when employing DPWM1 in a fixed-point digital platform, the word length of the  $\mu P$  or DSP can be more efficiently utilized. The other methods require a significant amount of data shifting to process the large inverse gain values such that overflow does not

occur and this results in poor modulation signal resolution and increased computation time. The inverse gain function data of DPWM1 can be easily fit into several first order polynomials leading to a smaller memory size requirement and improved accuracy. Near the six-step operating point ( $M_i \geq 0.99$ ) the gain inverse coefficients increase due to the rapid gain reduction and the inverse gain function can be better modeled by several data entries.

Employing the analytical gain function of DPWM1 and accounting for PEM based nonlinearity, the inverse gain function data can be accurately and easily computed from (4.44). Utilizing this data to obtain a simple hybrid model consisting of several piece-wise first order polynomial functions and several data entries is a straightforward task.

Compared to the direct digital PWM implementation, the triangle intersection technique requires simpler overmodulation algorithms. In the direct digital method, the overmodulation condition is detected only after computing a zero state time length with negative sign. Therefore, a back step for correcting the sign is inevitable, and additional algorithms (often complex) must be employed to compensate for the gain loss [75]. Therefore, DPWM1 triangle intersection method requires the simplest overmodulation algorithm and has superior performance when compared to all the other PWM methods reported.

## 4.7 Waveform Quality

As discussed in the previous chapter in detail, the linear modulation range harmonics of carrier based PWM methods (characteristic harmonics) are concentrated at the carrier frequency, its multiples and their sidebands. These harmonics could be successfully modeled with the HDF function. The analysis and comparison aided understanding the characteristics of all the modern modulators. It was illustrated that CPWM methods have superior waveform quality in the lower linear modulation index region while the DPWM methods would perform better in the higher linear modulation index region. Therefore, it was concluded a modulation algorithm that selects SPWM or SVPWM in the lower linear modulation region and a suitable DPWM method in the remainder of the linear modulation region would yield an optimal drive performance. However, the overmodulation region waveform quality was not considered. In this section the overmodulation region waveform quality will be investigated.

In the overmodulation region, as the unmodulated portions of the modulation waves increase the characteristic harmonics decrease. Therefore, the high frequency harmonic content becomes less significant with increasing modulation index and eventually becomes zero at the six-step operating point. However, large amount of sub-carrier frequency harmonics (5th, 7th, etc.) are generated and as the six-step mode is approached these harmonics become increasingly dominant in determining the waveform quality. Since the overmodulation region implies loss of volt-second balance, in the carrier cycles that saturation occurs

the HDF formula is not applicable. Therefore, it is difficult to analytically model the overmodulation region waveform characteristics of a modulator and a numerical approach is more suitable. Defined in the following, the inverter output line to line voltage Weighted Total Harmonic Distortion (WTHD) factor is an appropriate measure in determining the modulator waveform quality both in the linear and overmodulation range.

$$WTHD = 100 \times \frac{\sqrt{\sum_{i=2}^n \left(\frac{V_{LLi}}{i}\right)^2}}{V_{LL1}} \quad (4.47)$$

In most AC motor drive and utility interface applications, the WTHD function is more meaningful than the conventional voltage THD definition in which the  $\frac{1}{i}$  weight factor is absent in the formula because the WTHD function accounts for the low pass filter characteristic of the load inductance automatically. Thus, a better measure for the current harmonic distortion. The WTHD function is carrier frequency dependent and the  $V_{LLi}$  terms are typically calculated by evaluating the PWM-VSI line to line output voltage data for one fundamental cycle (obtained by simulation) through FFT analysis.

In this study, line to line voltage WTHD curves for SVPWM and DPWM1 are calculated and compared. The inverter line to line voltage data of a PWM-VSI drive which employs the once per carrier regular sampling technique is generated by means of computer simulations. The simulation assumes a fundamental frequency of  $f_e = 60$  Hz. The carrier frequency  $f_s$  is 5 kHz in the DPWM1 case and 3.33 kHz in the SVPWM case. This implies equal inverter

average switching frequency in both methods. In order to illustrate the carrier frequency dependency of the WTHD function, the SVPWM case is evaluated for 5 kHz also. The harmonic voltages, accounting for all the dominant harmonics (up to  $3f_s$ ), were calculated by evaluating the 8192 data points by means of an FFT algorithm of the MATLAB [1] numerical computation software package.

The WTHD curves in Fig. 4.15 (a) illustrate the advantageous waveform characteristics of the DPWM1 method at high modulation including the over-modulation range. Under the equal inverter average switching frequency criteria, the harmonic distortion of DPWM1 is less than the SVPWM methods from  $M_i \approx 0.6$  to  $M_i \approx 0.95$  where both curves merge. Under an equal carrier frequency criteria, which implies a 50 % increase in the average switching frequency in the SVPWM case, the waveform quality advantage of SVPWM over DPWM1 is lost near  $M_i \approx 0.90$ .

Although they have different shapes and definitions, the HDF and WTHD performance indices yield similar conclusions in the linear modulation region. Since in the lower modulation index region the line to line voltage pulses become narrow, the 8192 data FFT analysis yields a result with limited accuracy while the HDF approach is exact and yields a higher accuracy waveform quality calculation. Also it should be kept in mind these approaches are difficult to mathematically relate and they should be independently utilized as required by the application.

The blanking time and minimum-pulse-width control algorithm dependent

inverter nonlinearities can cause significant harmonic distortion increase which is modulator dependent. Figure 4.15 (b) illustrates the increase in the harmonic distortion when a  $12\mu s$  MPW control algorithm (PEM) is employed in the above system. Although the harmonic distortion increases in all the cases, the relative increase in the DPWM1 case is significantly smaller than the SVPWMs. The data clearly indicates that the harmonic distortion of the SVPWM method significantly increases and the increase in the switching frequency worsens the harmonic distortion. Therefore, accounting for the MPW nonlinearity, the superiority of DPWM1 over SVPWM begins at a significantly smaller modulation index value than the ideal case. Figure 4.15 (b) clearly indicates that if the carrier frequency is kept constant and the modulation method is switched from SVPWM to DPWM1 beyond  $M_i \approx 0.8$ , no degradation of waveform quality will be obtained relative to the SVPWM case. Furthermore, in the DPWM1 case the switching losses are greatly reduced.

Figure 4.15 also indicates the overmodulation region waveform characteristics of DPWM1 are superior to SVPWM until the point where the 5th, 7th, etc. sub-carrier frequency harmonics totally dominate and both WTHD curves merge ( $M_i \approx 0.95$ ). Although in the low end of the overmodulation range the WTHD factor is strongly dependent on the carrier frequency, inverter nonlinearities and the modulation method, in the high end it is dominated by the sub-carrier frequency harmonics and it is weakly dependent on the carrier frequency and the modulation method. Therefore, a detailed investigation of the sub-carrier frequency harmonic characteristics is required.

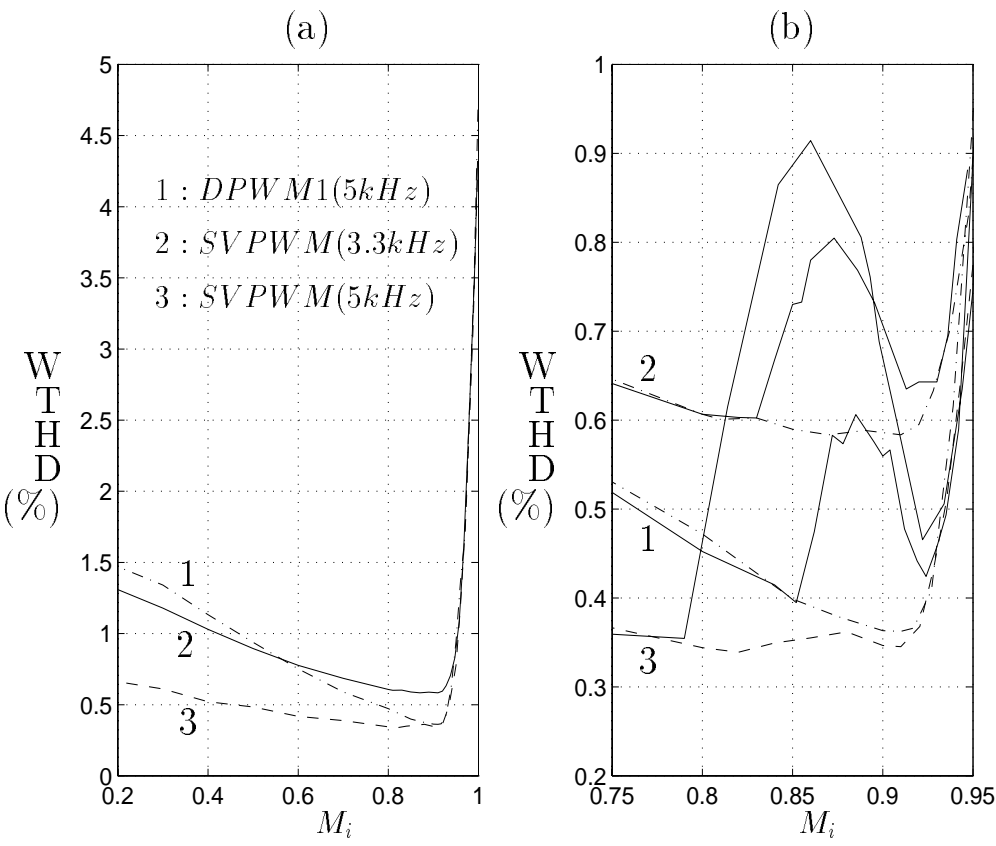


Figure 4.15: WTHD characteristics of SVPWM and DPWM1. (a): Ideal inverter model case. (b): Magnified view with MPW (solid) and without MPW (dashed) control algorithm.

### 4.7.1 Subcarrier Frequency Harmonic Content

Since each modulator has a unique modulation wave and in the overmodulation region unique modulation signals are generated, the sub-carrier frequency harmonic content of each modulator is unique. Since the modulation wave shape is independent of the carrier frequency, these harmonics are also independent of the carrier frequency. Although it is theoretically possible to closed form calculate these harmonics for each modulator, the process would be substantially difficult, laborious, and perhaps the detail unnecessary. Therefore, a numerical approach is more suitable to obtain the subharmonic data which is mainly required for the purpose of comparison between modulators.

For isolated neutral loads, the inverter output voltage subcarrier frequency harmonics which affect the drive performance are the non-triplen odd harmonics, i.e. 5th, 7th, etc. Since electric machines and utility interfaces with inductive interface filters have low pass filter characteristics, the high frequency inverter output voltage harmonics do not generate large currents, while small magnitudes of low frequency harmonics can generate large harmonic currents. As a result, the low frequency harmonics influence the drive characteristics at high modulation index values. They cause torque ripple and copper losses. Therefore, only the dominant low frequency harmonics need be considered.

In this study the overmodulation region inverter output voltage subcarrier frequency dominant harmonics are computed through FFT analysis of the modulation waves for various modulation index values. The 5th, 7th, 11th, 13th,

17th, 19th, 23th, and 25th harmonics are accounted for in this analysis. For each modulator and modulation index value, a full modulation wave fundamental cycle has been computed employing 2048 data points. Through FFT analysis of this data the harmonic components were calculated. Evaluating the individual harmonics, and excluding the triplen harmonics, the Total Harmonic Distortion (THD) (in (4.47), by replacing the  $\frac{1}{i}$  term with unity, the THD formula yields) was computed and stored for each modulation index and each modulator. For each modulator, the overmodulation range data has been evaluated for 20 different modulation index values. The results provide accurate estimates of the subcarrier frequency harmonic content for systems with carrier frequency to fundamental frequency ratios of approximately 20 or higher. For low ratios, the results are rough approximates. As illustrated in the voltage gain accuracy study, this limitation is due to the fact the actual discretized modulation wave may be slightly different than the ideal modulation signal. Since the carrier waves and switchings are not modeled, the data does not contain information regarding the carrier frequency harmonics. In the higher end of the overmodulation range, the influence of the high frequency harmonics on the total THD is significantly smaller than the low frequency harmonics, hence these terms can be neglected.

The voltage sub-carrier frequency THD characteristics of SVPWM, SPWM, THIPWM1/6, and DPWM1 have been calculated and shown in Fig. 4.16 in detail. The figure indicates that there is no significant difference between the THD of the zero sequence signal injection PWM methods considered. However, it is

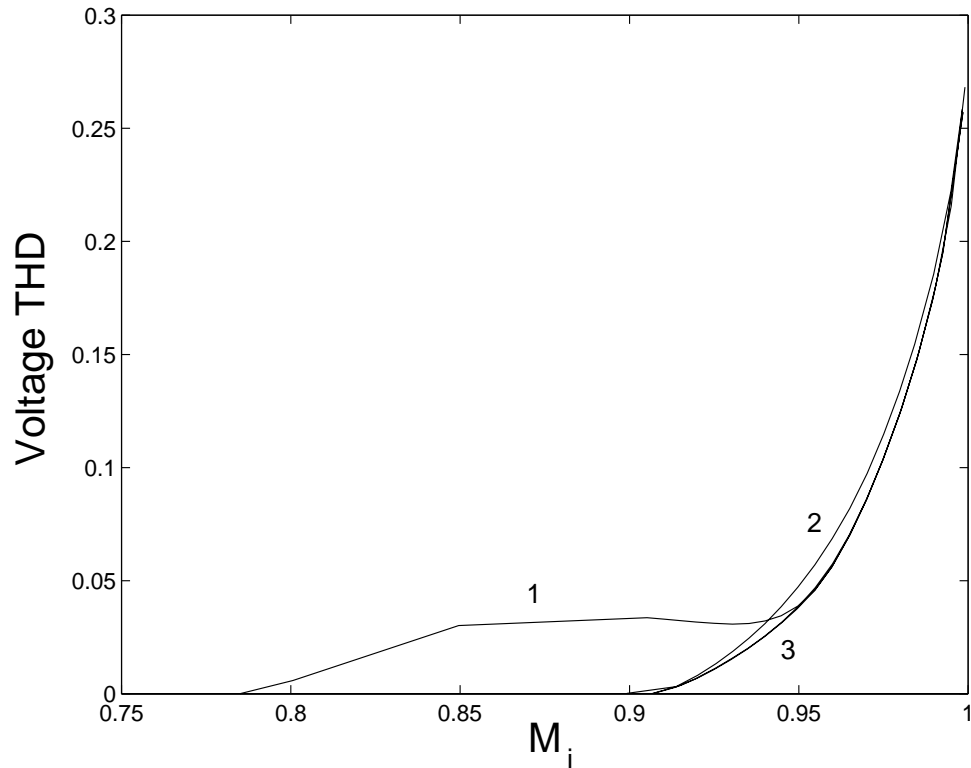


Figure 4.16: Ideal subcarrier frequency voltage THD of various modulators in the overmodulation range. 1: SPWM, 2:DPWM1, 3: SVPWM and THIPWM1/4.

visible from the curves that the SVPWM has slightly better THD characteristic. The SPWM method harmonic content has an interesting THD characteristic. As the modulator enters the overmodulation region the THD almost linearly increases, and at about 0.91 modulation index it saturates and furthermore it slightly decreases. As the modulation index further increases, the SPWM THD curve joins the other curves inclining towards the six step value.

Assuming that the AC load harmonic model can be represented by the load transient inductance, the current THD can be easily calculated from the voltage

harmonic data ( $I_n = \frac{V_n}{n\omega_e L_\sigma}$ ). If harmonic currents are a cause of concern from the efficiency or torque ripple perspective, the allowed overmodulation range of a drive may be limited to a modulation range in which the performance is acceptable. The harmonic characteristics extracted in this section can be utilized for such purposes.

Although the total voltage THD is very close in all the modulators discussed, the individual harmonics of various modulators may differ more noticeably. Figure 4.17, Figure 4.18, and Figure 4.19 show the modulation index dependency of sub-carrier frequency voltage dominant harmonics of the SPWM, DPWM1, and SVPWM. The data was calculated in terms of harmonic modulation index variables for the sake of generality. The figures indicate that the most dominant harmonic is the fifth harmonic, and as the order increases the harmonic magnitudes decrease. The dominant harmonics do not have linear gain relations with the modulation index value, and as the modulation index increases, their magnitudes increase very steeply, in particular near six step modulation. This characteristic is common to all the modulators discussed. The six-step operating mode harmonic content is well defined and these harmonics are the non-triplen odd harmonics. Utilizing the Fourier analysis approach, the harmonic content of the six-step voltage waveforms can be calculated as follows.

$$V_n = \frac{2}{n\pi} V_{dc} \quad (4.48)$$

where

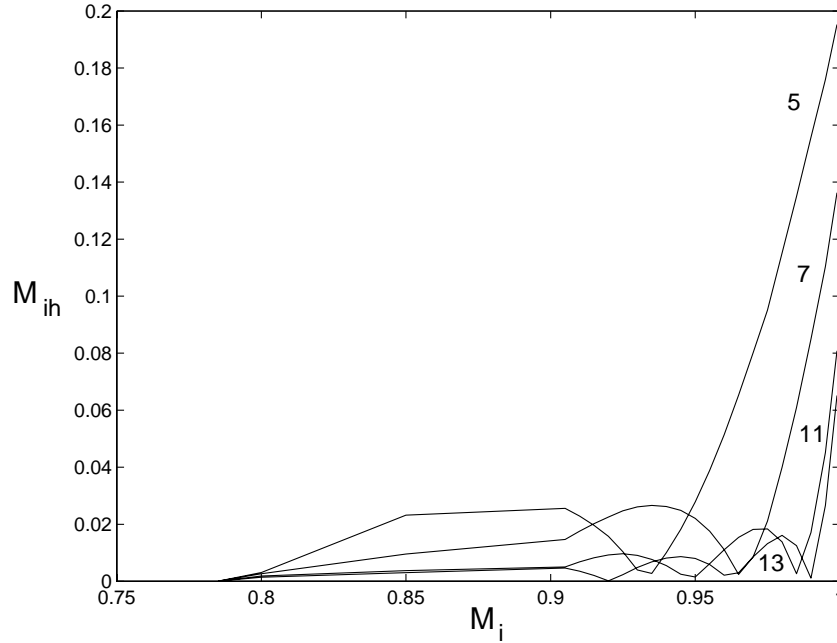


Figure 4.17: Individual voltage harmonic content of SPWM in the overmodulation range. The values are given in terms of the modulation index.

$$n = 6h \pm 1, h = 1, 2, 3, \text{ etc.} \quad (4.49)$$

### 4.7.2 Evaluation and Comparison

Inverter output voltage waveform quality in the lower end of the overmodulation region is mainly determined by the carrier frequency harmonics, and a modulator with less distortion would provide the best results. Therefore, selecting a suitable DPWM method would yield a superior performance. In the higher end of the overmodulation region, the sub-carrier frequency harmonics dominate the performance. Although the sub-carrier frequency harmonic content of different modulators is different, practically the voltage THD is not modulator type

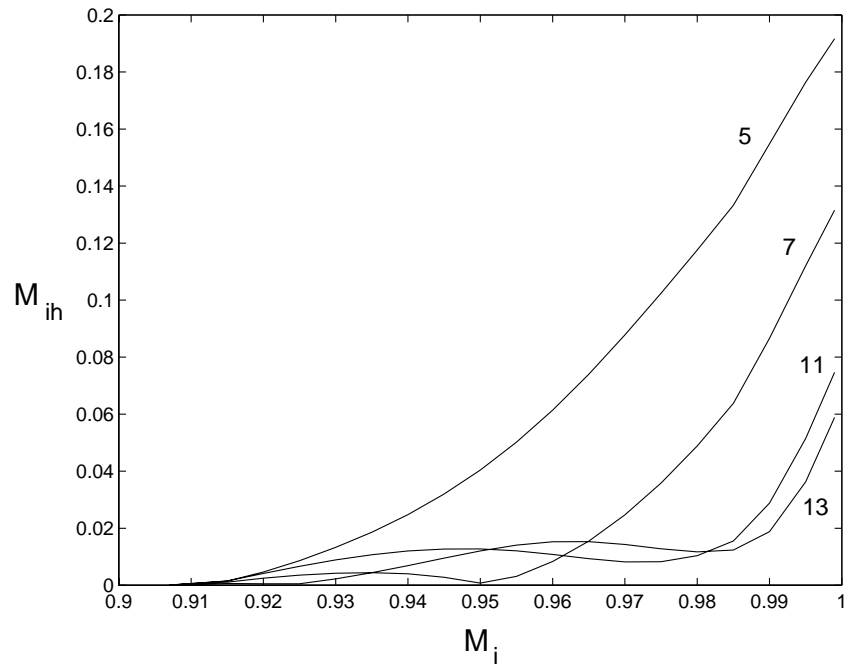


Figure 4.18: Individual voltage harmonic content of DPWM1 in the overmodulation range. The values are given in terms of the modulation index.

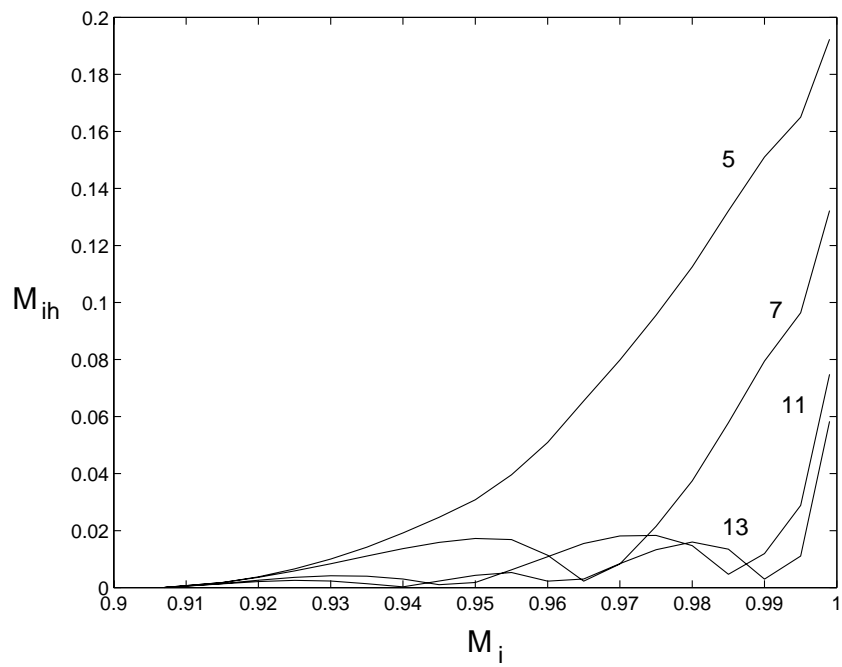


Figure 4.19: Individual voltage harmonic content of SVPWM in the overmodulation range. The values are given in terms of the modulation index.

dependent (except in comparison with SPWM which is considered a poor over-modulation method). Therefore, the choice of modulator in this region could be determined by other performance criteria such as voltage gain and switching losses. The modulation index value that the dominance of the carrier frequency harmonics ends and the sub-carrier frequency harmonics become dominant is approximately 0.95.

Since the harmonic current is approximately proportional to the inverse of the load transient impedance (at high frequencies mainly inductance), a load with large transient inductance experience less current ripple in the high over-modulation range than the low inductance loads. Therefore, it may be acceptable for some applications to allow the drive to operate in the overmodulation range, perhaps until 0.95 modulation index and even higher. Loads with large transient inductance can easily suppress the harmonics generated in the low end of the overmodulation range. In current ripple sensitive low inductance loads, the operating region perhaps could be limited to this value or less such that the overmodulation region drive performance does not significantly degrade. Since all modulators have essentially the same waveform quality beyond 0.95 modulation index, in this region the modulator choice could involve optimization of other performance indices such as the gain and switching losses.

In the previous chapter it was shown all DPWM methods have approximately equal HDF in the higher end of the linear modulation region. This argument is also valid for the switching frequency harmonics of the modulation

wave in the overmodulation region. Therefore, in the overmodulation region the waveform quality of all the discussed DPWM methods is practically the same as DPWM1 which has been investigated in this chapter. Since these results are also applicable to GDPWM at any modulator phase angle, an alternative to DPWM1 could be considered for switching loss reduction. However, transition from one operating point to another in the overmodulation region may result in substantial transients due to the differences in the voltage gain characteristics. Therefore, due to its superior voltage gain characteristic, the choice of DPWM1 from the beginning of the overmodulation region until the six-step operating mode is favorable. This result clearly indicates that for voltage feedforward drives, DPWM1 provides optimal performance in the overmodulation region from the global perspective of waveform distortion minimization, maximum voltage gain, and switching losses, and minimum transients. The overmodulation region experimental results of a voltage feedforward controlled drive are provided next.

## 4.8 Experimental Results

In this section the experimental voltage gain characteristics of SPWM, SVPWM, and DPWM1 are extracted and their waveform characteristics are illustrated. For this purpose, an experimental system which consists of a PWM-VSI drive and a 10 HP induction machine has been utilized. The inverter drive employs triangle intersection technique based PWM and the carrier frequency is 5 kHz.

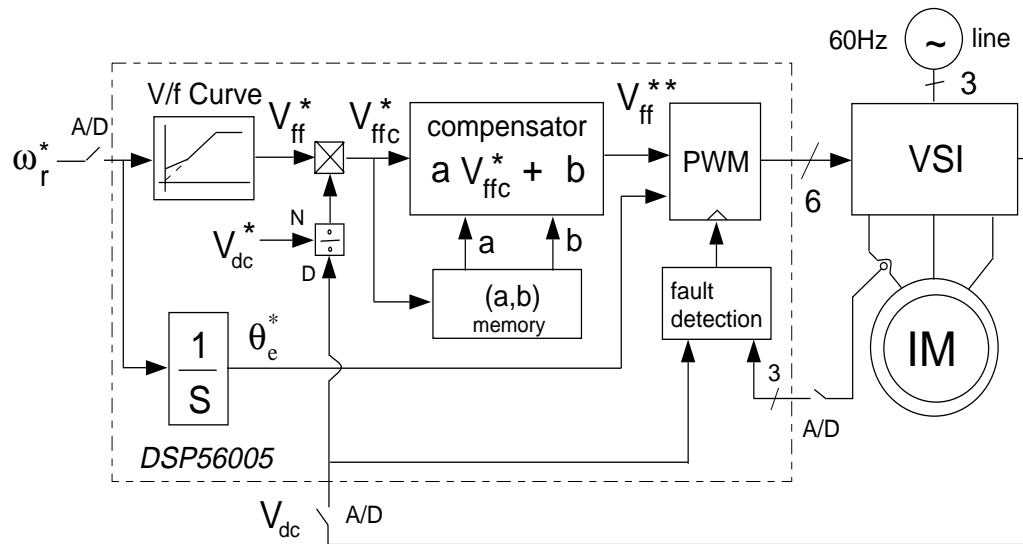


Figure 4.20: The experimental setup and the gain linearized DPWM1 based  $\frac{V}{f}$  controlled motor drive block diagram.

The blanking time of the inverter is  $4\mu s$ . The controller is fully digital and it employs a 24 bit fixed point DSP (Motorola 56005) with 40 MHz clock frequency [80]. The experimental system diagram is shown in Fig. 4.20 in detail.

For the purpose of voltage gain measurement, operating the drive in the constant  $V/f$  mode is adequate and the motor can be operated at no-load. The  $V/f$  algorithm and the modulation waves are generated by the DSP. In particular, generation of all the discussed modulation waves, exact blanking time compensation, and when required MPW control are all simple tasks requiring only a few lines of software code when employing a DSP. The digitally implemented triangle comparison hardware (PWM block) is also inside the DSP chip providing a compact integrated solution.

First, the SPWM and SVPWM method voltage gain characteristics were

extracted by measuring the reference and output line-line voltages from zero voltage until the six-step mode could be reached. The inverter output voltage fundamental component value was measured by a dynamic signal analyzer (HP35670A). The inverter DC bus voltage was also measured in order to account for the utility line and load dependent DC bus voltage variations. The test was conducted with and without PEM based MPW control algorithm. When employed, PEM eliminates (drops) the pulses which are narrower than  $12\mu s$ . Experimental results are shown in Fig. 4.21 along with the analytical results. As the figure clearly indicates, the theoretical and experimental results match with good accuracy. The SVPWM method has wider linearity range than the SPWM method, and both methods require very large reference signals in order to reach the six-step mode. As the experimental data indicates, PEM narrows the linearity range of both modulators quite significantly.

In the second stage, the gain characteristics of DPWM1 were measured, first without PEM control, and second with  $12\mu s$  PEM control. In the following, an inverse gain algorithm was implemented for the PEM controlled case and gain data extracted. Selecting the MPW length as  $12\mu s$ , the inverse gain function data was computed from (4.44) and this data was utilized to extract the following numerical approximation for the inverse gain compensated modulation index function.

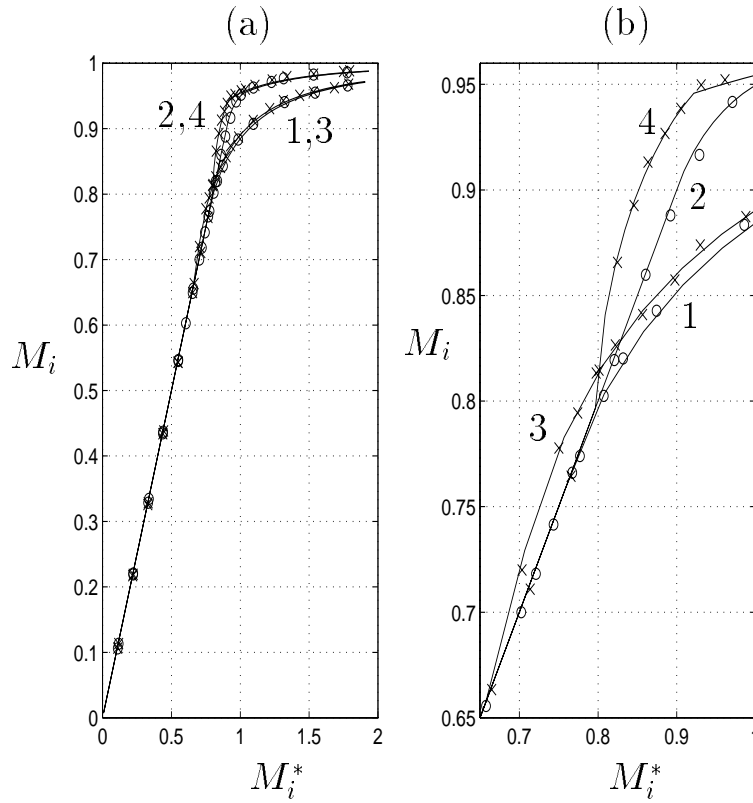


Figure 4.21: Experimental and theoretical  $M_i = f(M_i^*)$  characteristics of SPWM and SVPWM. (a): Full modulation range, (b): Magnified view of the nonlinear modulation region. 1: SPWM, 2: SVPWM, 3: SPWM with MPW, 4: SVPWM with MPW. The experimental data is shown with “o”, and “x” symbols, while the continuous curves correspond to the theoretical formulas.

$$M_i^{**}(M_i^*) = \begin{cases} M_i^* & 0 < M_i^* < 0.852, \\ 0.5252M_i^* + 0.4026 & 0.852 < M_i^* < 0.88 \\ 1.0823M_i^* - 0.0887 & 0.88 < M_i^* < 0.91 \\ 1.6659M_i^* - 0.6191 & 0.91 < M_i^* < 0.94 \\ 3.4396M_i^* - 2.2903 & 0.94 < M_i^* < 0.97 \\ 7.9754M_i^* - 6.6882 & 0.97 < M_i^* < 0.99 \\ 1.247 & 0.99 < M_i^* < 0.992 \\ 1.285 & 0.992 < M_i^* < 0.994 \\ 1.335 & 0.994 < M_i^* < 0.996 \\ 1.422 & 0.996 < M_i^* < 0.998 \\ 1.49 & 0.998 < M_i^* < 0.999 \\ 1.547 & 0.999 < M_i^* < 0.9993 \\ 1.65 & 0.999 < M_i^* < 0.9995 \\ 1.81 & 0.9995 < M_i^* < 1.0 \end{cases} \quad (4.50)$$

The above numerical representation provides a straightforward and highly accurate approximation with little computation and memory requirements, suitable for microprocessor or DSP implementations. In the gain linearized case, a DC bus voltage disturbance decoupling algorithm which scales the reference modulation index by  $\frac{V_{dc}^*}{V_{dc}}$  was also implemented in order to account for the DC bus voltage variations. The  $\frac{V_{dc}^*}{V_{dc}}$  value was computed by a simple Taylor series approximation ( $\frac{1}{1+x} \approx 1 - x + x^2$ ) instead of straightforward division which consumes significant amount of computations. The complete block diagram of

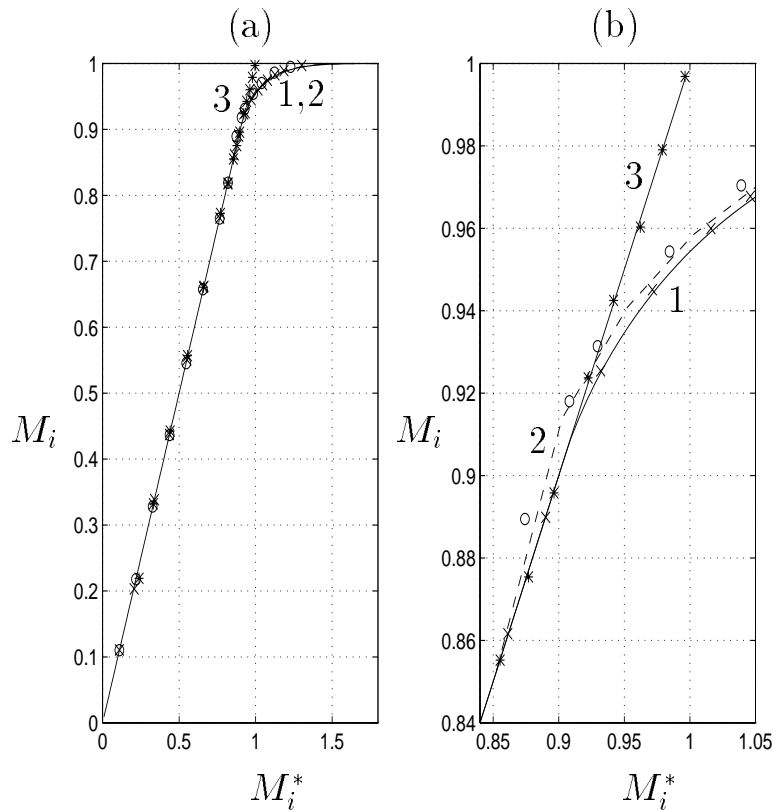


Figure 4.22: Experimental and theoretical  $M_i = f(M_i^*)$  characteristics of DPWM1 with and without linearization (a) and the magnified view of the overmodulation region (b). 1: The theoretical  $M_i = f(M_i^*)$  curve, 2: The theoretical  $M_i = f(M_i^*)$  curve with MPW, 3: Ideal linear modulator line. The experimental results are shown with “o”, “x”, and “\*” symbols.

the system for this case is shown in Fig. 4.20.

Figure 4.22 shows the theoretical and experimental gain characteristics of the DPWM1 method. The linearity range of the DPWM1 method as the data indicates is wider than the SVPWM case, and the influence of the MPW algorithm is significantly smaller. The gain compensator, as shown in the figure extends the modulator linearity until near the six-step operating mode with high accuracy.

For the purpose of comparing the waveform quality of DPWM1 and SVPWM, the motor currents for several modulation index values are demonstrated along with the modulation waveforms. The modulation signals were output from the DSP through a D/A converter and the triangular wave gain is  $\frac{20V}{V_{dc}^*}$  ( $\pm 10V$  represent the positive/negative DC rail clamp conditions). Figure 4.23 and Figure 4.24 illustrate the motor current and modulation waveforms of SVPWM and DPWM1 for  $M_i^* \approx 0.75$ . As the figures indicate, both modulators have good waveform quality within the linear modulation range and the ripple of SVPWM is slightly less. However, as the modulation index is increased and MPW control is applied the SVPWM performance degrades significantly. Figure 4.25 shows when a  $12\mu s$  PEM is employed, the SVPWM method performance degrades at  $M_i^* \approx 0.82$ , a value significantly smaller than the theoretical linearity limit of 0.907. The modulator linearity is lost at  $M_i^* \approx 0.82$  and the current waveform contains significant low frequency harmonic distortion leading to poor motor performance. As illustrated by the  $M_i^* \approx 0.855$  operating point in Fig. 4.26, DPWM1 maintains linearity and low harmonic distortion in a significantly wider modulation range. As illustrated in Fig. 4.27 by the  $M_i^* \approx 0.876$  operating point, beyond  $M_i^* \approx 0.855$ , modulator linearity is lost and the waveform quality significantly degrades. Further increase in the modulation index results in significant increase of the low frequency subcarrier harmonic content. Figure 4.28 illustrates the near six-step mode behavior of the inverter.

Notice in all the figures which belong to the high modulation region, the PWM ripple current magnitude appears to be practically the same. Since the

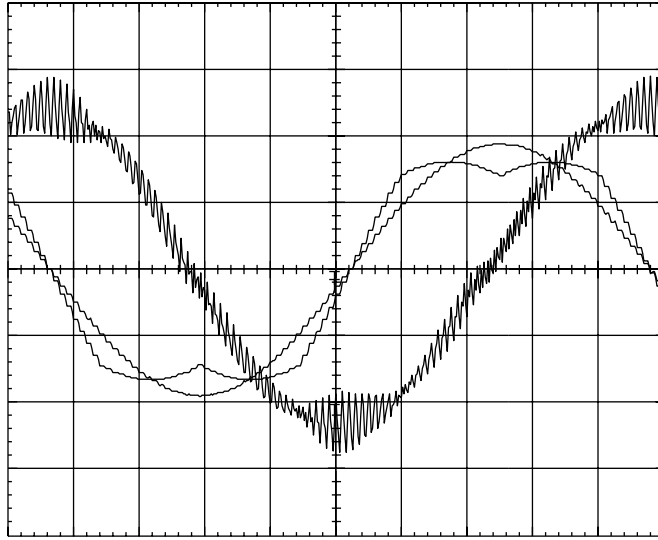


Figure 4.23: Experimental SVPWM modulation wave, its fundamental component and the motor current waveforms for  $M_i^* = 0.75$ . Scales: 2ms/div, 2A/div, 5V/div.

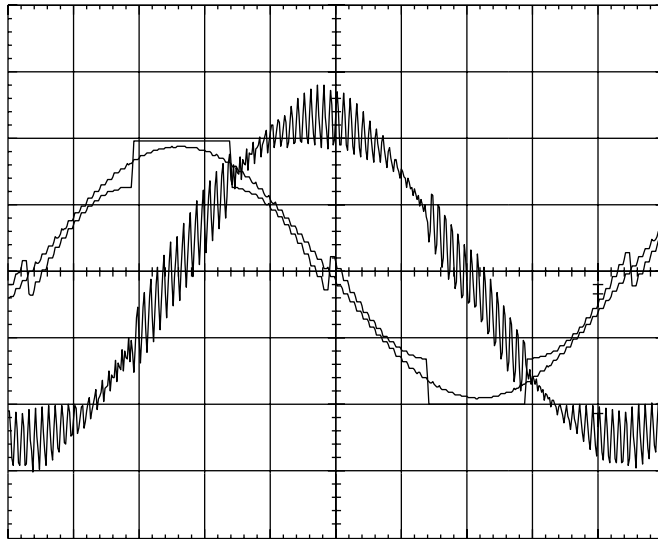


Figure 4.24: Experimental DPWM1 modulation wave, its fundamental component and the motor current waveforms for  $M_i^* = 0.75$  value. Scales: 2ms/div, 2A/div, 5V/div.

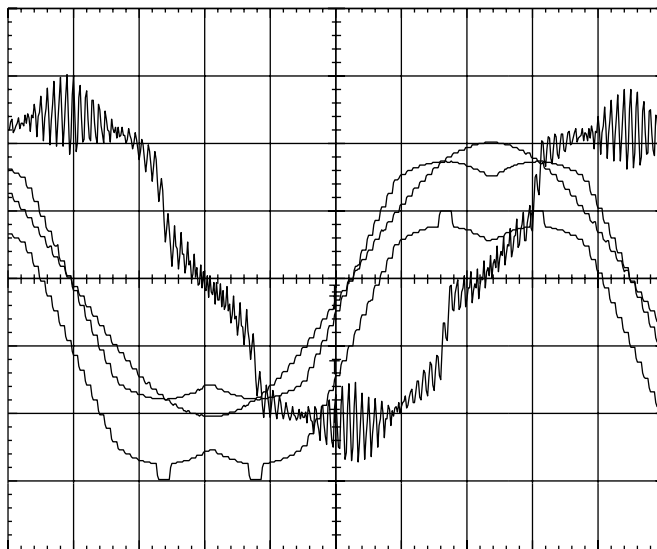


Figure 4.25: Experimental SVPWM modulation wave, modulation signal previous to MPW block, its fundamental component and the motor current waveforms for  $M_i^* = 0.82$ . Note the low frequency current harmonic distortion. Scales: 2ms/div, 2A/div, 5V/div.

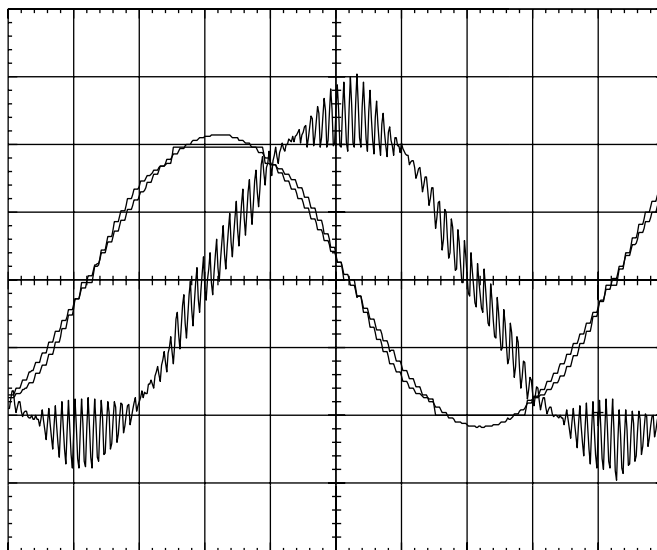


Figure 4.26: Experimental DPWM1 modulation wave, its fundamental component and the motor current waveforms for  $M_i^* = 0.855$  value. Scales: 2ms/div, 2A/div, 5V/div.

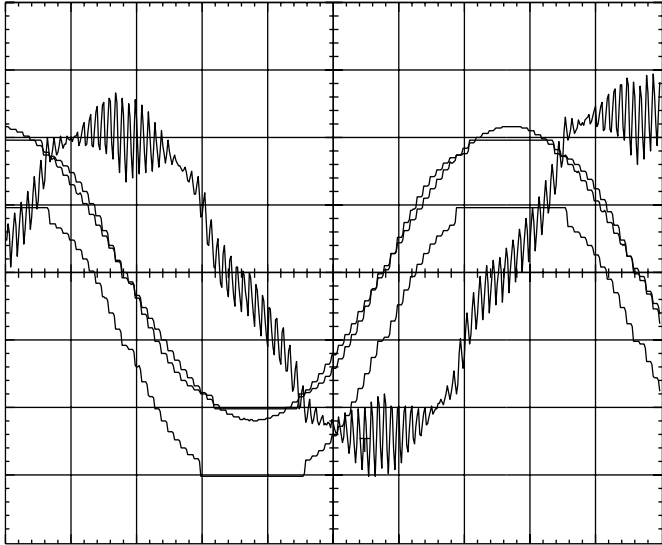


Figure 4.27: Experimental DPWM1 modulation wave, modulation signal previous to MPW block, its fundamental component and the motor current waveforms for  $M_i^* = 0.876$ . Scales: 2ms/div, 2A/div, 5V/div.

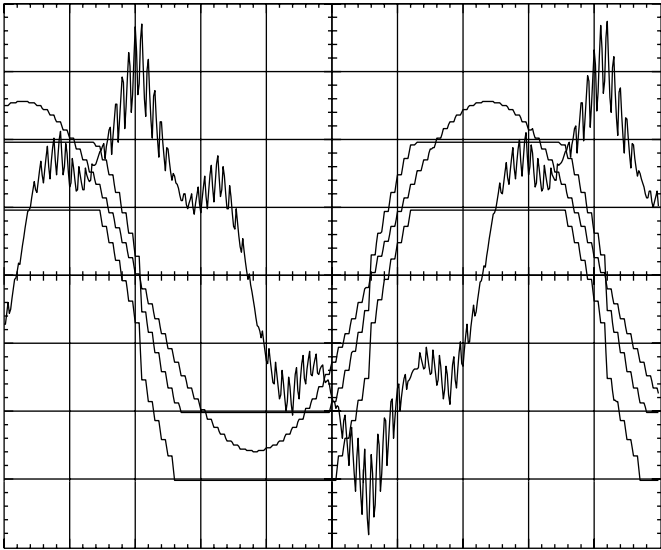


Figure 4.28: Experimental DPWM1 modulation wave, modulation signal previous to MPW block, and the motor current waveforms for  $M_i^* = 0.964$ . Note near the six-step mode the low frequency subcarrier harmonics are dominant. Scales: 2ms/div, 2A/div, 5V/div.

carrier frequency is fixed at 5 kHz for both SVPWM and DPWM1, the average switching frequency of DPWM1 is 33 % less than SVPWM. Therefore, DPWM1 has significantly reduced switching losses compared to SVPWM. Considering the reduction in the switching losses and increase in the linear modulation range, the DPWM1 method, clearly becomes the choice for operating in the high modulation range.

Finally, the sensitivity of the  $V/f$  controlled drive to DC bus voltage variations is illustrated with and without the inverse gain compensation and DC bus disturbance decoupling algorithms. The  $V/f$  controlled induction machine was operated at constant inverter output voltage reference value  $V_{1m}^* = 337$  V ( $M_i^* = 0.855$  at  $V_{dc}^* = 620$  V). Obtained from a diode rectifier, the DC bus voltage of the drive was slowly varied by adjusting the AC input voltage via an autotransformer and the motor terminal voltage was measured. Figure 4.29 illustrates the experimental inverter output voltage-DC bus voltage characteristics with and without inverse gain compensation and DC bus voltage disturbance decoupling. As the figure indicates, the compensated case output voltage is maintained at the commanded value until the DC bus voltage is significantly reduced and the inverter operates in the six-step mode. The uncompensated case output voltage significantly changes with the DC bus voltage variation. The motor speed and torque deviate from the normal operating points and poor drive performance results. Therefore, the compensated drive performance is insensitive to the DC bus voltage variations for a wide range of DC bus voltage variations (utility line voltage sag or surge conditions), while

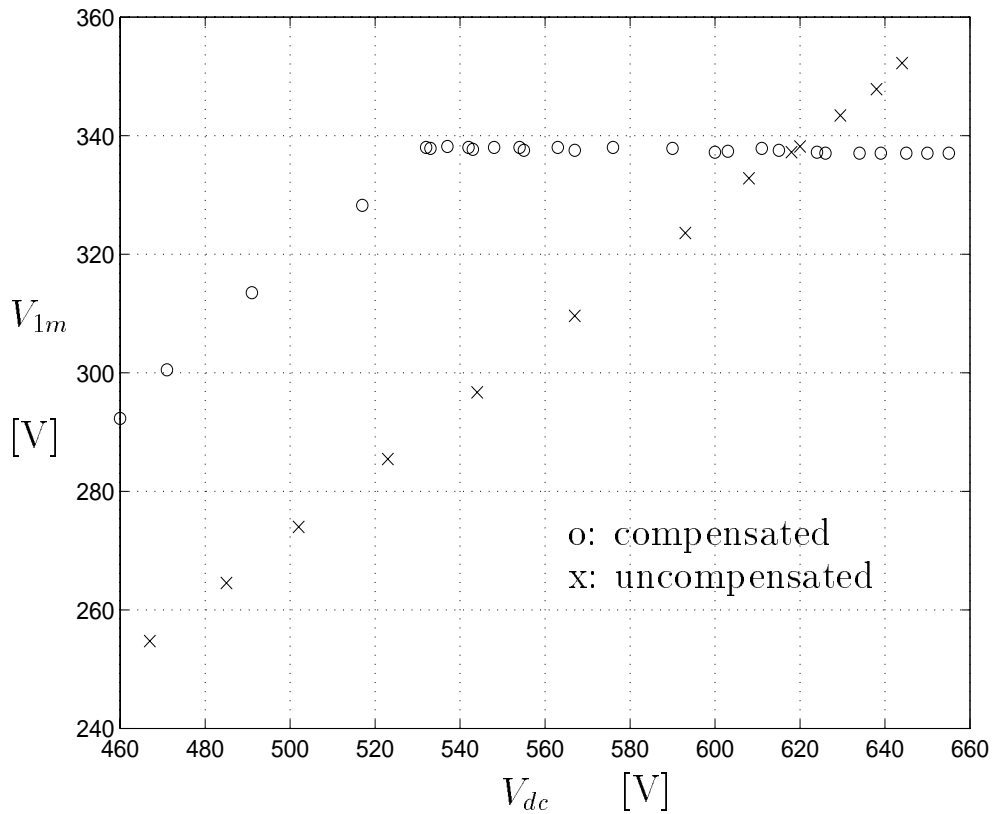


Figure 4.29: Experimental drive terminal voltage-DC bus voltage characteristics for  $V_{1m}^* = 337$  V.

the uncompensated drive experiences disturbances.

## 4.9 Voltage Feedforward PWM-VSI Drive High Performance Modulator Design

In the previous chapter the linear modulation region performance analysis of modern modulators indicated SPWM or SVPWM could provide superior performance in the lower linear modulation region and GDPWM and DPWM3

have superior attributes in the remainder of the linear modulation region. As this chapter illustrated the superior overmodulation region performance characteristics of DPWM1 (as a unique operating point of GDPWM), the conceptual stage of a high performance modulation algorithm design has been completed for voltage feedforward drives. The remaining task in the high performance modulation algorithm design procedure is to select appropriate modulation methods, determine the modulation method transition points and establish the control algorithm.

To maximize the drive performance, the transition point from SPWM/SVPWM to GDPWM and the  $\psi$  value of GDPWM must be properly selected. As the previous chapter indicated, the transition point from SPWM/SVPWM to GDPWM is determined by the waveform quality characteristics while the GDPWM modulator phase angle  $\psi$  is determined from the switching loss and voltage gain characteristics. Figure 4.30 shows the on-line modulator selector flow diagram of the proposed algorithm. Simple in structure and computational procedure, the algorithm requires only two transition modulation indices and  $\varphi$  as optimization parameters. With  $\varphi$  on-line estimated, the algorithm on-line calculates the optimal  $\psi$  to maximize the drive performance.

The transition value  $M_{itr2}$  is determined by the GDPWM linearity limit from (3.54) for  $k_m = 1$ . However, the optimal value of  $M_{itr1}$  depends on the carrier frequency value as well as the SLF and HDF characteristics. To assist in selecting this transition value, the HDF curves of SVPWM and GDPWM for

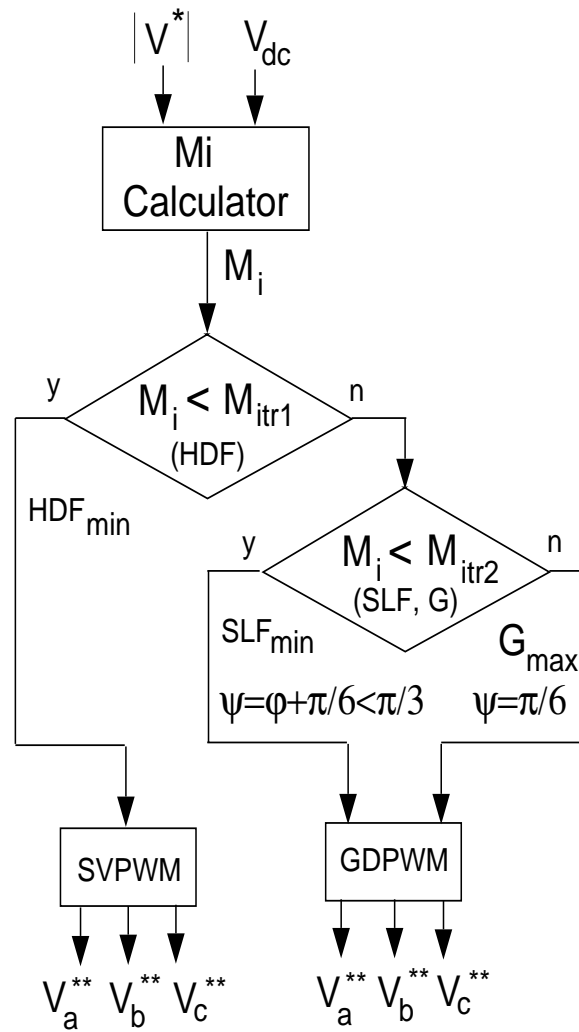


Figure 4.30: The combined high performance PWM algorithm flow diagram.

various carrier frequency values are compared in Fig. 4.31 for  $\psi = \frac{\pi}{4}$  (approximate average value over  $0 \leq \psi \leq \frac{\pi}{3}$ ). As the figure indicates, depending on the carrier frequency value, three practical cases can be distinguished.

1) Constant carrier frequency ( $f_c = \text{const.}$ ): As Fig. 4.31 indicates the theoretical HDF curves of SVPWM and GDPWM do not intersect and SVPWM is superior to GDPWM until  $M_{itr1}$  (calculated from (3.54) for  $k_m = 2$ ). As a result, transition from SVPWM to GDPWM at a point before  $M_{itr1}$  implies an increase in the current waveform distortion. However, according to Fig. 3.21 with early entrance to GDPWM, the switching losses can be reduced by as much as 50%. If the waveform quality requirements are not stringent, the  $M_{itr1}$  value should be selected as small as possible. Given a HDF limit, the  $M_{itr1}$  transition point can be easily determined from Fig. 4.31. More precise calculations to determine its value could involve (3.42) and (3.54).

2) Constant inverter average switching frequency ( $f_{swave} = \text{const.}$ ): In this case, the carrier frequency for SVPWM case is selected as  $f_c$ , and for GDPWM as  $1.5f_c$ , such that the inverter average switching frequency,  $f_{swave}$  remains constant. The HDF curves of Fig. 4.31 indicate the intersection point of SVPWM and GDPWM is at  $M_{itr1} \approx 0.65$ . Therefore, this  $M_{itr1}$  value minimizes the HDF of the drive, and under this condition the switching losses in the GDPWM mode are reduced by at most 25% when compared to SVPWM.

3) Constant switching losses ( $P_{swave} = \text{const.}$ ): In this case, the carrier frequency for SVPWM case is selected as  $f_c$ , and for GDPWM as  $2f_c$ , such that

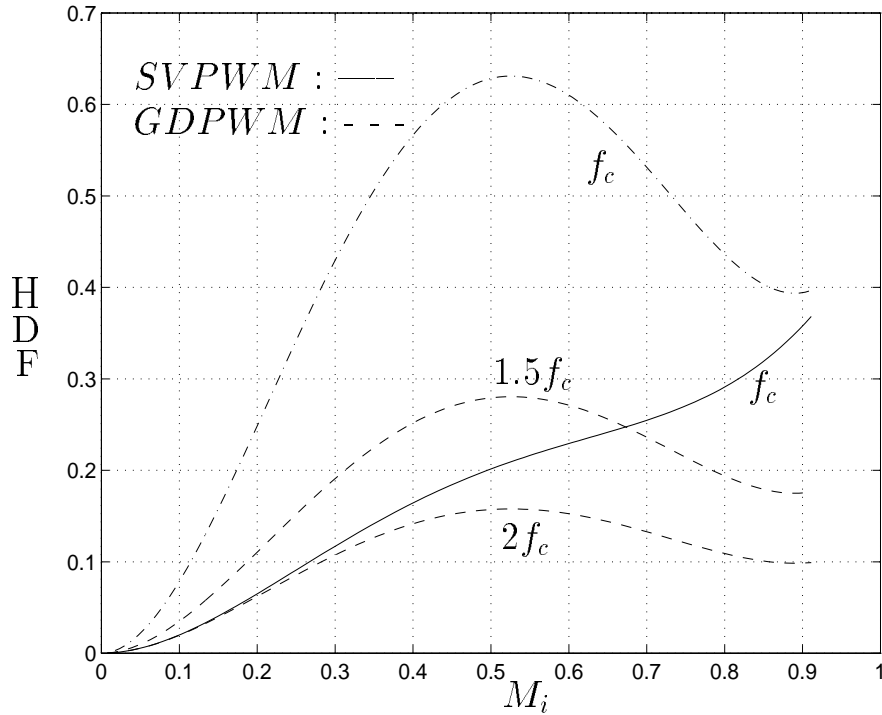


Figure 4.31:  $HDF = f(M_i)$  curves of SVPWM and GDPWM for various carrier frequency values illustrate the optimal transition points/regions.

the inverter switching losses  $P_{swave}$  remain constant (this is true for  $-30^\circ \leq \varphi \leq 30^\circ$  where the optimal SLF of GDPWM is 0.5). Figure 4.31 indicates that the SVPWM and GDPWM method curves are close together until near a modulation index of 0.3, then GDPWM method becomes superior. With this approach, smallest possible  $M_{itr1}$  becomes equal to the undermodulation limit of GDPWM defined in (3.55). Figure 4.31 indicates, in applications with small current ripple requirement,  $M_{itr1} \approx 0.3$  would yield superior performance. Note in this case SPWM can be utilized instead of SVPWM. Since at such low modulation levels SPWM and SVPWM have practically the same performance, SPWM can be chosen for its implementation simplicity.

The full PWM algorithm can be easily and efficiently programmed in a microprocessor or a DSP leading to a low cost high performance drive. Since the transition from SVPWM to GDPWM only involves a zero sequence signal, oscillatory transitions do not affect the load current fundamental component and motion control. Only the switching frequency harmonic content changes. The computational requirements of the algorithm (including the modulation signal generation) are only slightly higher than the conventional modulation methods. Thus, the algorithm is suitable over a wide range of applications where low cost, high performance, and high energy efficiency are in demand. Perhaps, the most suitable applications of the combined algorithm are the future generation multi-purpose intelligent drives. With the controller tuning the modulator on-line for the application, or by allowing the user to configure the modulator of his/her choice, an increased level of performance and satisfaction to the customer would result. Therefore, it is believed this algorithm will be an indispensable feature of future generation drives.

Linear modulation region performance of the above described high performance modulation algorithm was illustrated in the previous chapter by laboratory experiments. The present chapter experimentally illustrated the DPWM1 overmodulation region performance with a different motor from the motor utilized in the experiments of the previous chapter. The overmodulation region performance of the above described modulation algorithm with the previously utilized motor will next be presented for the sake of completeness.

## 4.10 Experimental Results of GDPWM in the Overmodulation Region

The high performance modulation algorithm combining SVPWM in the low modulation region, and GDPWM from the transition modulation index until the six-step operating point was tested in the laboratory and the linear modulation region performance was illustrated in the previous chapter. The overmodulation region performance of the drive with the same motor will be illustrated in this section. As described in the experimental results section of the previous chapter, with  $12\mu s$  minimum pulse width control (PEM) the GDPWM voltage linearity ends at 0.854 modulation index (calculated from (3.54)). However, the experimental study indicated transition at 0.86 modulation index value did not cause noticeable waveform quality degradation. Therefore,  $M_{itr2} = 0.86$  was selected. As a result, within  $0.81 < M_i < 0.86$  the GDPWM method reduces the switching losses significantly and maintains high waveform quality. Above  $M_{itr2}$  the GDPWM algorithm on-line selects  $\psi = \frac{\pi}{6}$  for maximum voltage gain, and the inverse gain compensated and DC bus voltage disturbance rejected modulator operates in the overmodulation range.

Figure 4.32 and Figure 4.33 show the modulator and motor phase current waveforms during and after transition to the nonlinear modulation range ( $M_i = 0.86, 0.903$ ). As the figures indicate the zero sequence signal oscillation (sudden variation of  $\psi$ ) does not distort the fundamental component current, and motion

quality is not affected. As the HDF curves of Figure 3.17 suggest, in the upper linear modulation range the phase current ripple of GDPWM decreases as the modulation index increases. In the overmodulation range the switching losses are reduced by at least 40% when compared to SVPWM. As the modulation index is further increased large amount of non-triplen odd subcarrier frequency voltage/current harmonics are generated and the waveform quality degrades due to inverter saturation. However, as Figure 4.34, and Figure 4.35 indicate, the modulated segments of the current waveform still retain the low harmonic distortion characteristic of the GDPWM method.

Figure 4.36 and Figure 4.37 illustrate and compare the effect of the PEM algorithm on the SVPWM and GDPWM method performance. As the experimental waveforms indicate, with 12  $\mu s$  PEM, the SVPWM method loses linearity at a lower modulation index than GDPWM method and the phase current waveform distorts significantly. As all the experimental waveforms indicate, the SVPWM method in the lower modulation range combined with the GDPWM method in the remainder of the range is a superior approach.

## 4.11 Summary

Closed form fundamental component voltage gain formulas of the conventional carrier based PWM methods, which are useful tools in the analysis and design

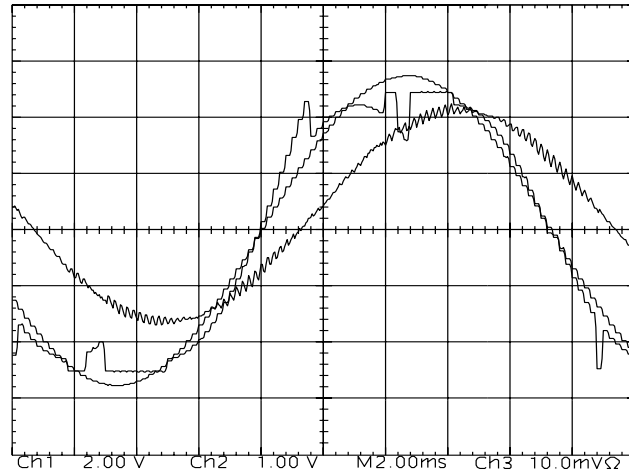


Figure 4.32: Transition of GDPWM from  $\psi = \varphi$  to  $\psi = 0$  ( $M_i = 0.86$ , 54 Hz,  $100\%T_{eR}$ ). Scaling: 5 A /div, 2 V /div, 2ms/div.

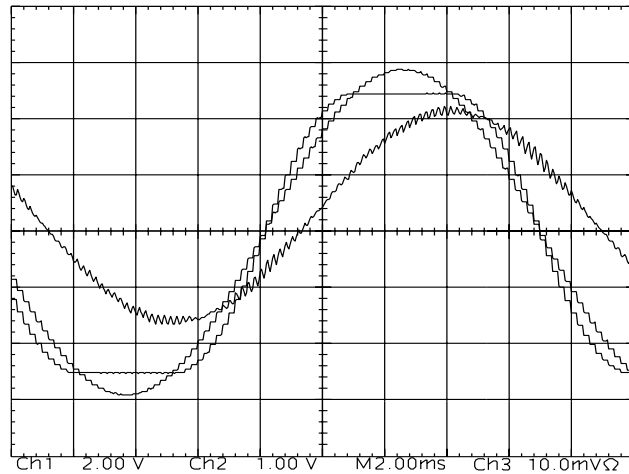


Figure 4.33: Experimental GDPWM modulation wave, its fundamental component and the motor current waveforms ( $M_i = 0.903$ , 56 Hz,  $100\%T_{eR}$ ). Scaling: 5 A /div, 2 V /div, 2ms/div.

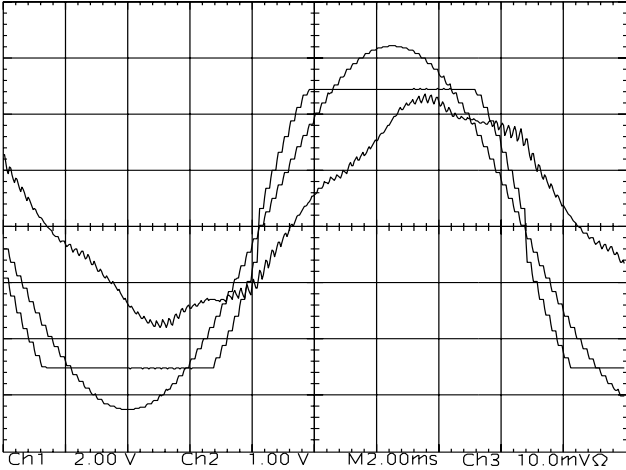


Figure 4.34: Experimental GDPWM modulation wave, its fundamental component and the motor current waveforms in the overmodulation range ( $M_i = 0.96$ , 59 Hz,  $100\%T_{eR}$ ). Scaling: 5 A /div, 2 V /div, 2ms/div.

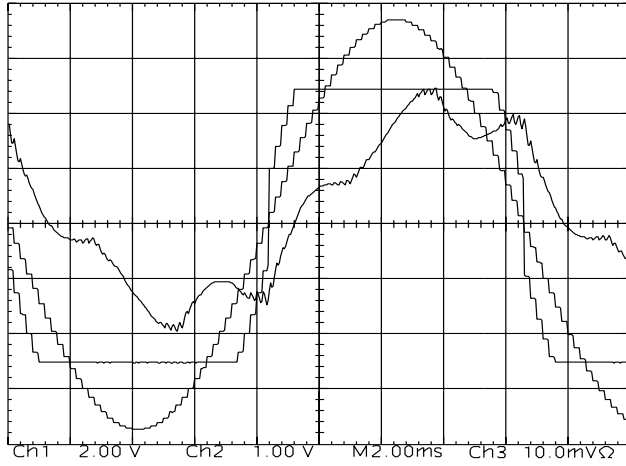


Figure 4.35: GDPWM modulation wave and motor current waveforms in the overmodulation range ( $M_i = 0.986$ , 60 Hz,  $100\%T_{eR}$ ). Scaling: 5 A /div, 2 V /div, 2ms/div.

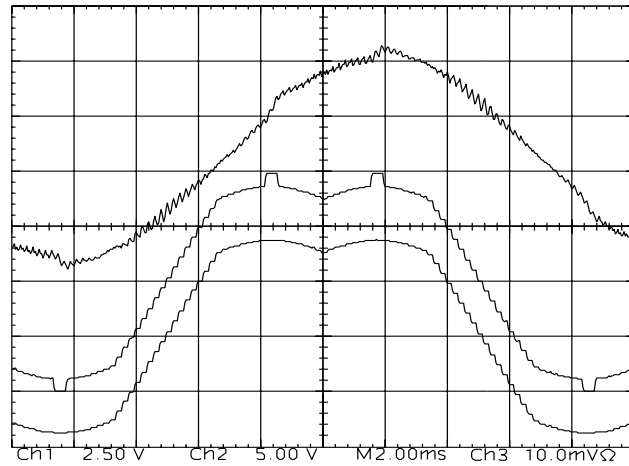


Figure 4.36: SVPWM modulation wave, PEM controlled modulation wave and the motor current waveforms for  $M_i = 0.815$ , 49 Hz. Scaling: 5 A /div, 2 V /div, 2ms/div.

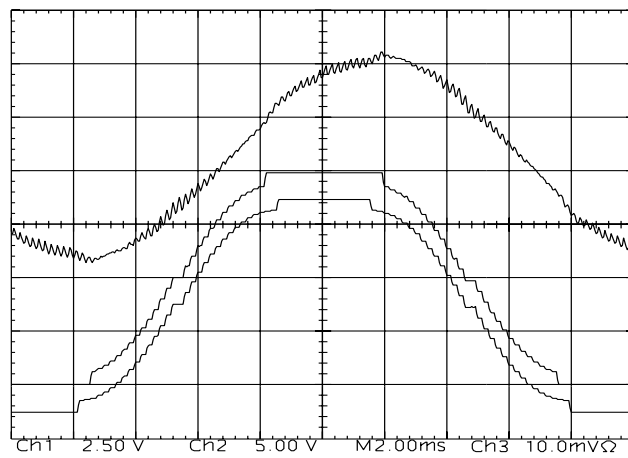


Figure 4.37: GDPWM modulation wave, PEM controlled modulation wave and the motor current waveforms for  $M_i = 0.867$ , 53 Hz. Scaling: 5 A /div, 2 V /div, 2ms/div.

of PWM-VSI drives were derived. High modulation index operating range voltage gain characteristics of various conventional carrier based PWM methods were analyzed and comparative results provided. Overmodulation region waveform characteristics of various PWM methods were numerically investigated and compared. The study indicates the DPWM methods have wider linearity range than the CPWM methods. The overmodulation range performance characteristics of DPWM1 are shown to be superior to the remainder of the known modulators. The voltage gain of DPWM1 is exceptionally high and its harmonic distortion is low.

It is shown that the inverter blanking time and minimum pulse width control based nonlinearities can significantly influence voltage gain and harmonic distortion characteristics of a modulator. MPW control significantly reduces the linearity range and increases the harmonic distortion. The effect is less significant in DPWM methods compared to CPWM methods.

The study indicates that for best overall performance a combination of various modulators must be employed: In the low modulation index range SVPWM has lower harmonic distortion. In the high modulation index range DPWM methods have wider linearity and less harmonic distortion. In the high linear modulation region the superiority of GDPWM was illustrated in the previous chapter. Therefore, in the overmodulation region, selecting the DPWM1 operating point of GDPWM results in optimal performance.

Voltage gain linearization is a simple task with DPWM1, and a polynomial

curve fit based inverse gain function in most of the region, and a small table entry near six step was found to be adequate to provide good linearity in the overmodulation range. The simplified inverse gain compensation and DC bus disturbance decoupling algorithms linearize the modulator with high accuracy and result in high drive performance.

Experimental voltage gain and waveform characteristics are in good agreement with the theoretical predictions, and illustrate the performance superiority of GDPWM over SVPWM in the high modulation and overmodulation range (in particular of DPWM1).

Finally, the high performance modulator design rules for voltage feedforward controlled drives were established and a high performance modulation algorithm which combines SVPWM and GDPWM was developed. Simple design formulas and graphics, which overly simplify the voltage feedforward drive modulator design procedure were established.

The next chapter addresses the overmodulation issues of closed loop current controlled PWM-VSI drives. With the dynamic performance requirements of current controlled drives being substantially higher than voltage feedforward drives, these drives differ in design and performance than the voltage feedforward drives. Therefore, the subject is of significant importance and will be thoroughly investigated in the remainder of this thesis.